Nongyrotropic electrons in guide field reconnection

D. E. Wendel, M. Hesse, N. Bessho, M. L. Adrian, and M. Kuznetsova

Articles you may be interested in

Phase space structure of the electron diffusion region in reconnection with weak guide fields
Phys. Plasmas **19**, 112108 (2012); 10.1063/1.4766895

Electric field structure inside the secondary island in the reconnection diffusion region
Phys. Plasmas **19**, 042902 (2012); 10.1063/1.3700194

Model of electron pressure anisotropy in the electron diffusion region of collisionless magnetic reconnection
Phys. Plasmas **17**, 122102 (2010); 10.1063/1.3521576

Electron acceleration during guide field magnetic reconnection
Phys. Plasmas **15**, 032903 (2008); 10.1063/1.2876465

Fast collisionless reconnection in electron-positron plasmasa)
Phys. Plasmas **14**, 056503 (2007); 10.1063/1.2714020

Nongyrotropic electrons in guide field reconnection

D. E. Wendel,[1] M. Hesse,[1] N. Bessho,[1,2] M. L. Adrian,[1] and M. Kuznetsova[1]
[1]*NASA Goddard Space Flight Center, Greenbelt, Maryland 20771, USA*
[2]*University of Maryland, Baltimore County, Baltimore, Maryland 21250, USA*

We apply a scalar measure of nongyrotropy to the electron pressure tensor in a 2D particle-in-cell simulation of guide field reconnection and assess the corresponding electron distributions and the forces that account for the nongyrotropy. The scalar measure reveals that the nongyrotropy lies in bands that straddle the electron diffusion region and the separatrices, in the same regions where there are parallel electric fields. Analysis of electron distributions and fields shows that the nongyrotropy along the inflow and outflow separatrices emerges as a result of multiple populations of electrons influenced differently by large and small-scale parallel electric fields and by gradients in the electric field. The relevant parallel electric fields include large-scale potential ramps emanating from the x-line and sub-ion inertial scale bipolar electron holes. Gradients in the perpendicular electric field modify electrons differently depending on their phase, thus producing nongyrotropy. Magnetic flux violation occurs along portions of the separatrices that coincide with the parallel electric fields. An inductive electric field in the electron $\mathbf{E} \times \mathbf{B}$ drift frame thus develops, which has the effect of enhancing nongyrotropies already produced by other mechanisms and under certain conditions producing their own nongyrotropy. Particle tracing of electrons from nongyrotropic populations along the inflows and outflows shows that the striated structure of nongyrotropy corresponds to electrons arriving from different source regions. We also show that the relevant parallel electric fields receive important contributions not only from the nongyrotropic portion of the electron pressure tensor but from electron spatial and temporal inertial terms as well. © *2016 AIP Publishing LLC*. [http://dx.doi.org/10.1063/1.4942031]

I. INTRODUCTION

Magnetic reconnection is a phenomenon that alters magnetic topology and converts stored magnetic energy into particle energy in charged plasmas. The process by which this occurs is still a topic of debate and investigation. A parallel electric field $E_\parallel$ with certain properties is necessary to violate the frozen-in flux condition, and to break the conservation of field lines.[1,2] Except at the smallest relevant spatial scales, that of the electron skin depth, the gradients in electron pressure tensor shears largely balance the parallel electric field.[3–8] These pressure shears manifest themselves as deviations from gyrotropic symmetry about the magnetic field. Therefore, understanding the production of nongyrotropic electron populations is important to improving both theoretical models and observations of reconnection.

Signatures of electron nongyrotropy in the context of magnetic reconnection have recently been observed in space[9,10] and in simulations.[3,5,11–18] Chen et al.[9] see electron gyrophase signatures consistent with nongyrotropy in magnetotail reconnection with very little guide field, while Scudder et al.[10] observe a high value of their agyrotropy parameter at guide field reconnection in the magnetopause. In simulations, Aunai et al.,[11] Karimabadi et al.,[7] Kuznetsova et al.,[13] Pritchett et al.,[14] Scudder et al.,[15] and Shuster et al.[16] observe and measure nongyrotropy in 2D or 3D antiparallel particle-in-cell (PIC) simulations of magnetic reconnection, while Hesse,[12] Hesse et al.,[3] Hesse et al.,[5] and Scudder et al.[15] do so for guide field reconnection. Hesse[12] and Hesse et al.[3,12] estimate the effects of electron

nongyrotropy at the field-reversal region, while Scudder et al.[15] use a scalar measure of nongyrotropy they base on only two of the eigenvalues of the electron pressure tensor, as do Karimabadi et al.[7] and Pritchett et al.[14] for the antiparallel case. Here, we use the scalar measure of electron nongyrotropy based on all three eigenvalues of the nongyrotropic pressure tensor as defined by Aunai et al.[11] in a PIC study of nongyrotropic electrons along the inflow and outflow separatrices of antiparallel reconnection.

In their analysis of nongyrotropy, Aunai et al.[11] develop a scalar measure of nongyrotropy that takes into account all the information from the full 3D nongyrotropic pressure ellipsoid. Applying their measure to a 2.5D PIC simulation of symmetric antiparallel reconnection, they find that the nongyrotropy measure frames and localizes the electron diffusion region. Applying their measure to an antisymmetric, antiparallel 2.5D PIC simulation, they find that the nongyrotropy extends somewhat along the separatrices, but is maximized about the reconnection site. Their analysis of the outflow electron distributions reveals the conjunction of counterstreaming electron populations of different symmetries with respect to the magnetic field where the Hall B_y component reverses. The collocation of populations with different symmetry thus produces an overall lack of gyrotropic symmetry.

We apply the same measure, D_{NG}, to the electron pressure tensor in a 2.5D PIC simulation of symmetric reconnection with a guide field to locate enhanced nongyrotropy. To observe how electrons are nongyrotropic, we collect particle

distributions in field-aligned boxes in a layer that cuts across regions of nongyrotropy in the inflow and outflow. Furthermore, we examine the forces from relevant parallel and other non-ideal electric fields as well as electron trajectories to identify the sources and location of the nongyrotropic electrons.

The PIC simulation solves the Vlasov and Maxwell system of equations with an initial Harris-like, symmetric configuration in the x-z plane and a guide field $B_y = 1$, in units of the arbitrary background field B_0. The conditions for a Harris equilibrium are $B_0^2/(2\mu_0) = n_0(T_i + T_e)$ and $v_{di} - v_{de} = 2/(\lambda e B_0)(T_i + T_e)$, where v_{di} and v_{de} are the drift velocities in the out-of-plane y-direction for the ions and the electrons, respectively. Here, n_0 is the density at the initial peak of the Harris sheet, T_i and T_e are the ion and electron temperatures, respectively, and λ is the width of the Harris sheet, where $\lambda/d_i = 0.5$, $d_i = c/\omega_{pi}$ is the ion skin depth, and $\omega_{pi} = (n_0 e^2/\varepsilon_0 m_i)^{1/2}$ is the ion plasma frequency. The initial current sheet is defined by $B_x = B_0 \tanh(z/\lambda)$ and a normalized guide field of $B_y/B_0 = 1$, with reconnection initiated by a 3% X-type perturbation to the normal magnetic field. The density profile is $n = n_0 \operatorname{sech}^2(z/\lambda) + n_b$, where n_b is the background density and $n_b/n_0 = 0.2$. The grid size is 3200×3200 spanning 100 d_i along the outflow direction x and 50 d_i along the inflow direction z, and the time resolution is $0.1 = \omega_{pe}^{-1}$, where $\omega_{pe} = (n_0 e^2/\varepsilon_0 m_e)^{1/2}$ is the electron plasma frequency. The fields boundary conditions are periodic in x and conducting in z, while the particles are specularly reflecting in z. Magnetic fields are in units of the background field B_0, lengths in units of ion skin depth d_i, times in units of ion cyclotron period Ω^{-1}_{ci}, densities in units of the uniform background density n_0, electric fields in units of $v_A B_0$, currents in units of $j_0 = B_0/(\mu_0 c/\omega_{pi})$, and thermal pressures in units of B_0^2/μ_0. Here, v_A is the Alfvén speed $B_0/(\mu_0 m_i n_0)^{1/2}$, and $\Omega_{ci} = e B_0/m_i$ is the ion cyclotron frequency. There are 10^9 particles and the mass ratio is $m_i/m_e = 100$. Other defining parameters are $\omega_{pe}/\Omega_{ce} = 2$, $T_i/T_e = 5$, and $v_A/c = (m_e/m_i)^{1/2} \Omega_{ce}/\omega_{pe} = 1/20$. Further details on the numerical scheme are available in Ref. 4. In Section IV, we present particle trajectories. The trajectories are derived from a test particle integrated in the interpolated simulation fields. The orbit integration algorithm is the same as the one used in the actual PIC simulations and works backward in time, updating the fields every 20 ω_{pe}^{-1} for a duration of 100 ω_{pe}^{-1}, and interpolates the equations of motion to a resolution of 0.005 ω_{pe}^{-1}.

We will first discuss the identification of regions of enhanced nongyrotropy by applying to the simulation domain the scalar measure based on the electron pressure tensor. In Section III, we will establish the nonideal electric force environment present in the nongyrotropic regions. In Section IV, we will then sample electron distribution functions in a number of field-aligned boxes across regions of enhanced nongyrotropy along the electron inflow and outflow directions to observe the features and structures of the electron distributions as they change from gyrotropic to nongyrotropic. We will also show the results of particle tracing to identify the histories of the nongyrotropic particles to solidify their relationship with the local nonideal electric fields. In Section V, we demonstrate the electron nongyrotropy, and

in some locations, the electron inertia are essential to balance the observed large-scale parallel electric field.

II. NONGYROTROPY

The nongyrotropic part **N** of the pressure tensor is $\mathbf{N} = \mathbf{P} - \mathbf{P}_G$, where the gyrotropic part $\mathbf{P}_G = P_\perp \mathbf{I} + (P_{||} - P_\perp)\mathbf{bb}$, with **b** the unit vector along **B**. Here, $P_\perp$ and $P_{||}$ are, respectively, the perpendicular and parallel components of the pressure tensor in field-aligned coordinates, where $P_{||} = \mathbf{b} \cdot \mathbf{P} \cdot \mathbf{b}$ and $P_\perp = (tr(\mathbf{P}) - P_{||})/2$. Aunai *et al.*[11] propose a scalar measure of nongyrotropy based on the eigenvalues λ_i of **N** and is normalized by the thermal energy, $Tr(\mathbf{P}) = Tr(\mathbf{P}_G)$. These authors define the scalar measure, which they call D_{NG}, as

$$D_{NG} = \frac{\sqrt{\sum_i \lambda_i^2}}{Tr(P_G)} = \frac{\sqrt{\sum_{i,j} N_{i,j}^2}}{Tr(P_G)}, \qquad (1)$$

where in the last identity we have expressed the sum of the eigenvalues using the Frobenius norm. Using the Frobenius norm greatly reduces the number of numerical operations.

We apply this measure to the case with a guide field, which we show in Fig. 1 along with magnetic field lines, in white. In contrast to the antiparallel case, where D_{NG} is localized around the diffusion region,[11] Fig. 1 shows that D_{NG} extends outward from the diffusion region roughly parallel to the magnetic separatrices along both the inflow (lower left and upper right quadrants) and outflow (upper left and lower right quadrants). It forms a pair of bands in all locations and, in the outflow region at least, is not exactly parallel to the field lines, suggesting a time-of-flight effect is at play in forming those bands. Along the inflow regions, localized enhancements suggest patchiness superposed on the bands. In Sections III–V, we will derive an explanation for the structure of D_{NG} and determine how and why the corresponding electron distributions are nongyrotropic.
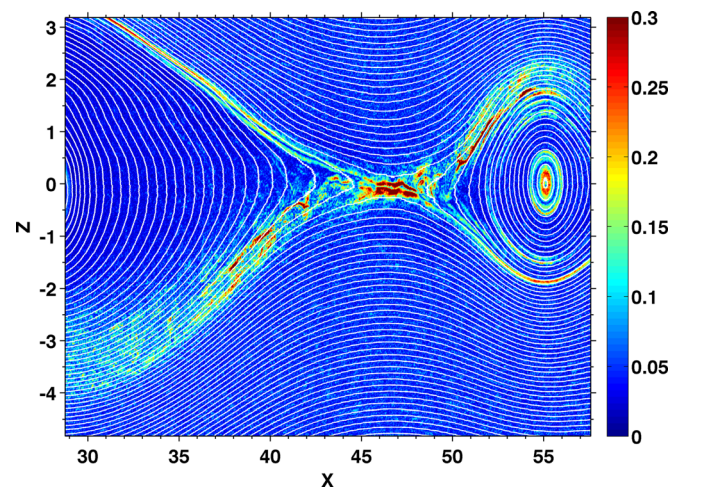

FIG. 1. The nongyrotropy parameter D_{NG} (color) is elevated not only in the diffusion region but also along the separatrices. It shows a striated structure everywhere. The magnetic field lines (white) are oriented toward the right in the upper half-plane, and the inflow separatrices lie in the lower left and upper right quadrants.

III. INFLUENCE OF THE ELECTRIC FIELD

Previous modeling and observational investigations of reconnection have revealed both large scale and, in the case of guide-field reconnection, small scale parallel electric field structures.[18–26] The small-scale structures take the form of electron holes and bipolar electric fields along the magnetic separatrices, where they are attributed to particle beam instabilities.[18,20,21,24,25] Existing research has also revealed large scale parallel potential drops connected to the reconnection region[19,21,23,28,29] that coexist with the localized bipolar fields when guide fields are present. From Wind and Cluster measurements and simulations of guide field and antiparallel reconnection, Egedal *et al.*[22,30] also find an in-plane trapping potential that emanates away from the x-line, consistent with observations from Cluster.[23] They find that the electric field integrated along field lines from the ambient plasma to the x-line produces a large-scale parallel potential that maximizes at the x-line and traps lower energy electrons.[30] The potential corresponds to a parallel electric field that points away from the reconnection region.

In common with the above studies, we find localized bipolar parallel electric fields as well as a large-scale net parallel potential drop on field lines entering and exiting the reconnection region. Fig. 2 shows localized electron holes. The parallel electric field is calculated from $\mathbf{E} \cdot \mathbf{B}/B$ averaged over sixty simulation time steps, where each time step corresponds to an evolution of the system over $0.1\ \omega_{pe}^{-1}$. The bipolar parallel fields congregate along the separatrices and are particularly strong along the separatrices aligned with the electron inflow. Observing the holes over time shows that they move away from the x-line along field lines, primarily along the out-of-plane direction.

An integration of the parallel electric fields along field lines from the end of the simulation domain to the x-line of our PIC simulation reveals a large-scale parallel potential along field lines entering and exiting the reconnection region of our simulation. Fig. 3 shows the integrated parallel electric field $\int_{-\infty}^{l} \mathbf{E} \cdot \frac{\mathbf{B}}{|\mathbf{B}|} dl$ along field lines threading the diffusion region. For clarity, only field lines along that have not yet reconnected or are just undergoing reconnection are included in the integration. The integration is performed
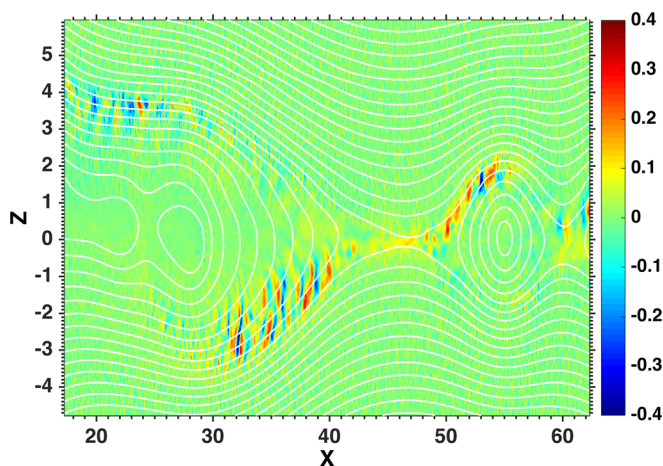

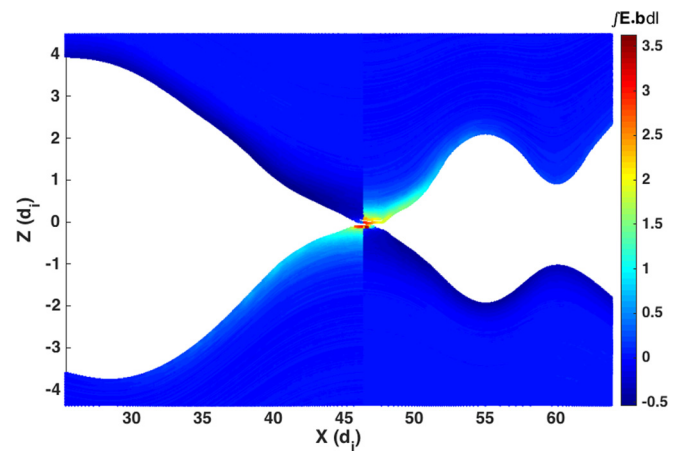FIG. 3. The integrated parallel electric field $\int_{\pm\infty}^{l} \mathbf{E} \cdot \frac{\mathbf{B}}{|\mathbf{B}|} dl$ along field lines threading the diffusion region. For clarity, only field lines along that have not yet reconnected or are just undergoing reconnection are included. The integration is performed from the left side toward the x-line along the portions of the field lines that lie in the left domain, and from the right toward the x-line along the portions of the field lines that lie in the right hand domain. A net negative value indicates an antiparallel electric field, and a net positive value a parallel electric field. Because **B** points to the right in the upper half-plane, and to the left in the lower half-plane, the parallel electric fields point away from the x-line in all quadrants.

from the left side toward the x-line along the portions of the field lines that lie in the left domain, and from the right toward the x-line along the portions of the field lines that lie in the right hand domain. Also note that this definition differs from the traditional definition in that the direction of dl is always the same as the direction of B. A net negative value indicates an antiparallel electric field, and a net positive value a parallel electric field. Because **B** points to the right in the upper half-plane, and to the left in the lower half-plane, the parallel electric fields point away from the x-line in all quadrants. While the parallel field that contributes to the net potential is weak in amplitude compared to the bipolar fields, the nonzero integrated value shows that it is persistent and collocated with the bipolar fields. The scale and polarity of the potential is consistent with previous results in the antiparallel case.[30] As in the previous work,[30] the net potential ramp along the outflow separatrix is much smaller than along the inflow separatrix. Along the inflow, the integrated parallel electric field starts to grow where the Hall magnetic field pulls the field line further out of the plane, supporting the view that the field line picks up the reconnection electric field as it grows in the $+y$ direction. The contribution of the reconnection electric field has been discussed in depth previously.[31] Though much smaller in magnitude, the large-scale parallel electric field coincident with the outflow separatrix (upper left, for example) opposes the direction of the reconnection electric field (which, because of the guide field, would be parallel to B) and therefore cannot be attributed to the total reconnection electric field. We shall return to this question in Section V, where we demonstrate how the terms of Ohm's law contribute to the nonideal electric field along the separatrices coinciding with the inflow and outflow directions.

One correction that can produce nongyrotropic electrons is related to electric field gradients. This phenomenon has

FIG. 2. The parallel electric field.

been observed in the context of shocks, where gradients of the electric field pointing in a direction perpendicular to **B** and parallel to a component of **E** induce an effective gyrofrequency $\omega_{c,eff}$ that differs from ω_c.[32,33] We will denote the portion of the electric field that arises from a gradient that satisfies these conditions as $\nabla_\perp \mathbf{E}_\perp \cdot \mathbf{r}_\perp$, where the perpendicular direction is defined with respect to **B** and **r** denotes a distance vector. For example, an electric field $\mathbf{E} = \mathbf{E}_0 + \mathbf{z}\partial E_z/\partial z$ that is orthogonal to **B** yields an effective gyrofrequency $\omega^2_{c,eff} = \omega^2_c - q/m\partial E_z/\partial z$ such that the effective gyroradius becomes $r_{eff} = v/\omega_{c,eff}$. Thus, it is possible to have values of the electric gradient that make the gyrofrequency effectively smaller and the gyroradius effectively much larger, allowing the particles to become nonadiabatic. For electrons, this occurs when $\nabla_\perp \mathbf{E}_\perp \cdot \mathbf{r}_\perp$ points in the same direction as **E**. Even if the gradient is in a sense that $\omega^2_{c,eff} > \omega^2_c$, the effect influences particles with different initial thermal speeds differentially, such that the ensemble can still become nongyrotropic. For moderate values of $\nabla_\perp \mathbf{E}_\perp \cdot \mathbf{r}_\perp$ and for electrons, $\omega^2_{c,eff} = \omega^2_c + e/m\partial E_z/\partial z$. Cole[32] shows that in the frame drifting with the electrons, the particles still gyrate, but the gyrations become elliptical and that the ellipse is offset at an angle relative to **B**. The gradient modifies the usual $\mathbf{E}_o \times \mathbf{B}$ drift in a way that depends on the initial particle thermal velocity perpendicular to **E** and **B** and on the initial particle gyrofrequency. Thus, particles with different speeds will drift differentially, and the direction of the drift will be determined by the sign of $\nabla_\perp \mathbf{E}_\perp \cdot \mathbf{r}_\perp$ relative to the direction of $\mathbf{E}_\perp$. Fig. 4(b) shows the in-plane components of the total electric field by black arrows and D_{NG} in color. Along the separatrices, especially the separatrices with the inflowing electrons, the in-plane **E** has a component perpendicular to **B** and also has a gradient along that same direction. At the locations of high D_{NG}, the gradients $\nabla_\perp \mathbf{E}_\perp \cdot \mathbf{r}_\perp$ are in the same sense as the direction of $\mathbf{E}_\perp$. They are generally positive in the vicinity of the elevated D_{NG}. In this case, the gyrofrequency will not be effectively reduced. However, the

nongyrotropic regions harbor gradients in the perpendicular electric field that are consistent with the possibility that these forces produce differential drift of electrons exposed to it, and therefore contribute to electron nongyrotropy.

Another contribution to the electron nongyrotropy along the separatrices comes from a nonzero curl of the nonideal electric field. The total nonideal electric field in the electron rest frame $\mathbf{E}_{NI} = \mathbf{E} + \mathbf{v}_e \times \mathbf{B}$ is shown for a small region along an inflow separatrix in Fig. 4(a). Here, the color again corresponds to the out-of-plane component $E_{NI,y}$, and the black vectors are the in-plane components. The in-plane components are also elevated along the electron holes, suggesting the presence of forces that could produce electron nongyrotropy. It is strongest on field lines that are reconnecting or have just reconnected. Furthermore, all three components of the curl of the nonideal electric field $\nabla \times \mathbf{E}_{NI}$, shown in Fig. 5, are nonvanishing along the separatrices and near the diffusion region. The condition $\nabla \times \mathbf{E}_{NI} = \frac{\partial \mathbf{B}}{\partial t} - \nabla \times (\mathbf{v}_e \times \mathbf{B}) \neq 0$ is a necessary and sufficient condition for violation of magnetic flux conservation (e.g., Ref. 34). The z component, $(\nabla \times \mathbf{E}_{NI})_z = \partial E_{NI,y}/\partial x$, reflects the bipolar structures of the electron holes. In contrast, the in-plane gradients that contribute to the x and y components, e.g., $(\nabla \times \mathbf{E}_{NI})_y = \partial E_{NI,x}/\partial z - \partial E_{NI,z}/\partial x$, where $\partial E_{NI,x}/\partial z$ dominates, produce structures coherent on large spatial scales along the separatrices and the y component exists in the diffusion region. The nonideal field is therefore rotational and has a strong rotational component perpendicular to z and y along the electron Larmor orbits gyrating about the magnetic field lines. We note here, however, that the strength of the nonideal effects along the separatrices is sensitive to the mass ratio and may be reduced at a more realistic mass ratio.[27]

Even if the particles do not slip further than a Larmor radius from the field line, this rotational component of $\mathbf{E}_{NI}$ will affect the gyration speed about the gyrocenter, which we call v_θ in cylindrical gyrocenter coordinates. Under certain conditions, it will also affect the azimuthal symmetry of v_θ, and
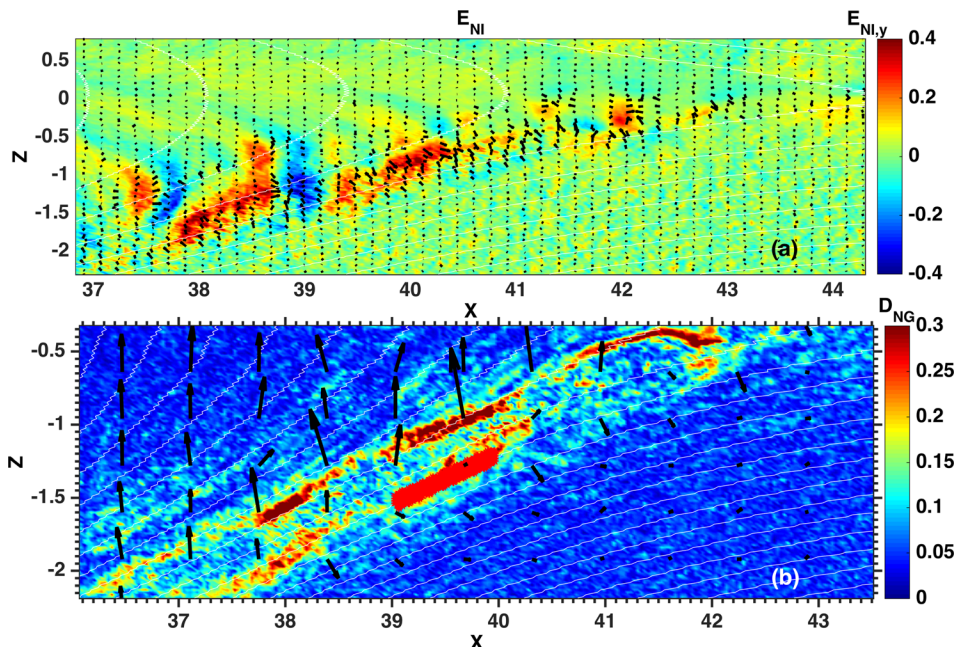

FIG. 4. (a) The total nonideal electric field $\mathbf{E} + \mathbf{v}_e \times \mathbf{B}$, the y-component in color and the in-plane components as black arrows. (b) The total electric field E poloidal components, black arrows, against the parameter D_{NG} in color. The red box is located at one of the distributions analyzed in this study.
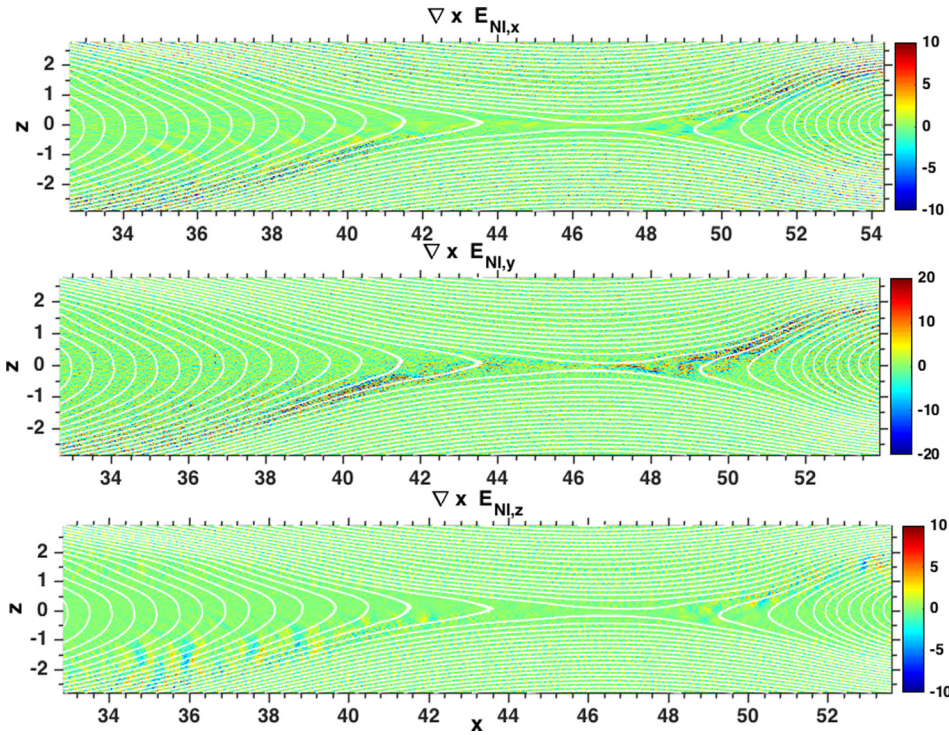
FIG. 5. $\mathbf{\nabla} \times \mathbf{E_{NI}} \neq \mathbf{0}$ along the magnetic separatrices, indicating an inductive electric field in the frame of the electron drift velocity.

thus the gyrotropy. In the electron gyrocenter coordinates, there is an effective emf $\int \mathbf{E_{NI}} \cdot d\mathbf{r} = \pm \int E_{NI,\theta} \cos(\phi) r_L d\theta$ on the path of the electron Larmor orbit, where $d\mathbf{r} = r_L d\boldsymbol{\theta}$ is an element of the orbit, r_L is the electron Larmor radius, φ is the angle between the plane of the rotational part of $\mathbf{E_{NI}}$ and the plane of the electron orbit, and the sign depends on whether $E_{NI}\cos(\phi)$ is parallel or antiparallel to the orbit. Even if we ignore electron inertial contributions to $\mathbf{E_{NI}}$ and neglect density gradients, the pressure divergence will produce a change in v_θ of $dv_\theta/dt = \pm e E_{NI,\theta} \approx \pm (-\mathbf{\nabla} \cdot \mathbf{P}_e)_\theta / n_e m_e = \pm [\omega_c/v_\theta \partial v_\theta^2/\partial\theta + \partial(v_\theta v_z)/\partial z]$. Here we have set v_r and terms containing it equal to 0, the radial coordinate $r = r_L = v_\theta/\omega_c$, and z to be along the direction of $\mathbf{B}$. If we assume that v_θ is uniform with θ and z, then $dv_\theta/dt = \pm v_\theta \partial v_z/\partial z$ and $v_\theta = v_{\theta,0} \exp[\pm \int_{t0}(\partial v_z/\partial z)dt]$. (We know that, and as we will demonstrate in Section IV, the parallel gradient in v_z exists because the electrons are accelerated along the field lines by the parallel electric fields.) If the direction of $\mathbf{E_{NI}}$ and the sign of $\partial v_z/\partial z$ are uniform over the gyroperiod, this has the consequence that the gyration speed will change more over time for those particles that have a larger parallel gradient in their parallel speed, but it does not yield any phase dependence and the electrons therefore remain gyrotropic (except there may be some dependence as to the phase of particles at t_0). However, if the sign of $\mathbf{E_{NI}} \cdot d\mathbf{r}$ or $\partial v_z/\partial z$ changes during an orbit, then part of the orbit will see a decrease in v_θ and part of the orbit will see an increase, thus producing a phase dependence and a nongyrotropy. As the bottom panel of Fig. 5 shows, $\mathbf{E_{NI}} \cdot d\mathbf{r}$ changes sign in conjunction with the holes (with the change in sign occurring in the middle of the potential wells). Therefore, particles that are fast enough to stream across the holes will encounter this effect as they cross the boundaries, so we would expect it to most influence those particles with the largest parallel velocities. The importance of this effect on the fast particles would

depend on how many gyrations occurred between encountering a change in $\mathbf{E_{NI}} \cdot d\mathbf{r}$. Moreover, as we discuss in Section IV, slower particles spend some time bouncing within the holes and therefore undergo a change in the sign of $\partial v_z/\partial z$ at each turning point of their bounce and a change in sign of $\mathbf{E_{NI}} \cdot d\mathbf{r}$ within the well during their transit. The result is that the particles with the largest parallel velocities within the hole—i.e., those that are traversing the minimum in the well where $\mathbf{E_{NI}} \cdot d\mathbf{r}$ changes sign, will become nongyrotropic at this juncture. Fig. 25(a) in the Appendix gives a heuristic picture of these two scenarios.

Now if we include dependence of v_θ on θ, for example, as might already exist from another source, such as the gradient $\mathbf{\nabla}_\perp \mathbf{E}_\perp \cdot \mathbf{r}_\perp$, then the above expression for dv_θ/dt includes the term $\pm \omega_c \partial v_\theta/\partial\theta$. This demonstrates that the curl of $\mathbf{E_{NI}}$ acts upon existing nongyrotropy. If, for example, there is an azimuthal bump in the distribution, then $\partial v_\theta/\partial\theta$ is positive on one side of the bump and negative on the other side of the bump (see Fig. 25(b) in the Appendix). Thus, with time, this term increases v_θ on one side of the bump and decreases it on the other. Finally, we point out that any component of $\mathbf{E_{NI}}$ that is not symmetric during an orbit, such as produced by a gradient in $\mathbf{E_{NI}}$ over the orbit, may serve to create further azimuthal asymmetries in the electron orbits about $\mathbf{B}$. The regions surrounding the boxes in Figure 4 reveal that gradients in $\mathbf{E_{NI}}$ exist over the boxes.

IV. ELECTRON DISTRIBUTIONS

To verify the sources of electron nongyrotropy, we collect distributions from boxes aligned with the magnetic field that span the sections of inflow and outflow with enhanced D_{NG}. In Fig. 6(a), the grid locations of the distributions are identified against the backdrop of D_{NG} (color) by numbered, colored boxes along the inflow (lower left) and outflow
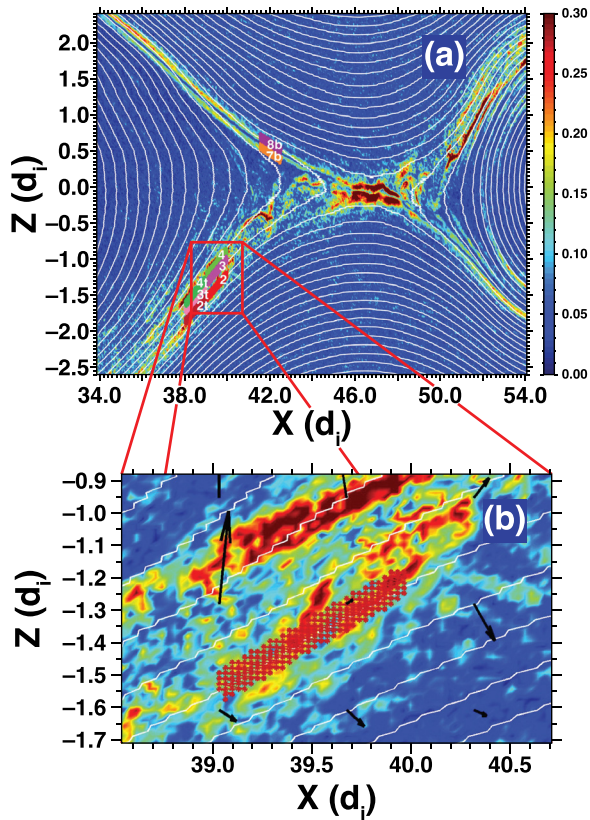
FIG. 6. (a) A region flanking the x-line with elevated D_{NG} (background color) and the boxes along the inflow (lower left) and outflow (upper left) where we take electron distributions. (b) A magnification of the lower left separatrix, with box 2 highlighted in red. This view shows the gap where we take boxes 3 and 3t, which lies between strips of elevated D_{NG}.

(upper left) in a region flanking the x-line. (A magnification of the lower left separatrix, in Fig. 6(b), shows box 2 highlighted in red. This view reveals the gap where we take boxes 3 and 3t between strips of elevated D_{NG}.) The boxes are 0.5 d_i high and 1.0 d_i wide and are chosen to be small enough to avoid aliasing and large enough to collect sufficient particles. Some boxes lie along different sections of the same field lines to match potential wells and hills in the parallel electric field. The final distributions are obtained from averaging distributions from 60 time steps in order to increase the number of particles and improve statistics. The distributions presented are *reduced* distributions, meaning that, to produce $F(v_x,v_y)$, for example, we have integrated the phase space distribution along v_z.

Fig. 7 shows the running average of D_{NG} and the density n_e, and $\varphi_{\parallel} \equiv -\int_{-\infty}^{x} \mathbf{E} \cdot \hat{\mathbf{b}} dl$ as a function of field line length l for the field lines containing boxes 2, 3, and 4. (Here, we plot the negative of the integral as plotted in Fig. 3 in order to show the potential as an electron would see it. Once again, this definition differs from the traditional definition in that the direction of d$\mathbf{l}$ is always the same as the direction of **B**.) From these curves, we can see that generally D_{NG} tends to grow and n_e tends to decrease as $|\varphi_{\parallel}|$ increases. The black dashed line through the center of box 4t, for example, ties the hole with a local peak in D_{NG} and enhancements in n_e at the edges of the hole. Fig. 8, a magnified view of these quantities for the field line containing
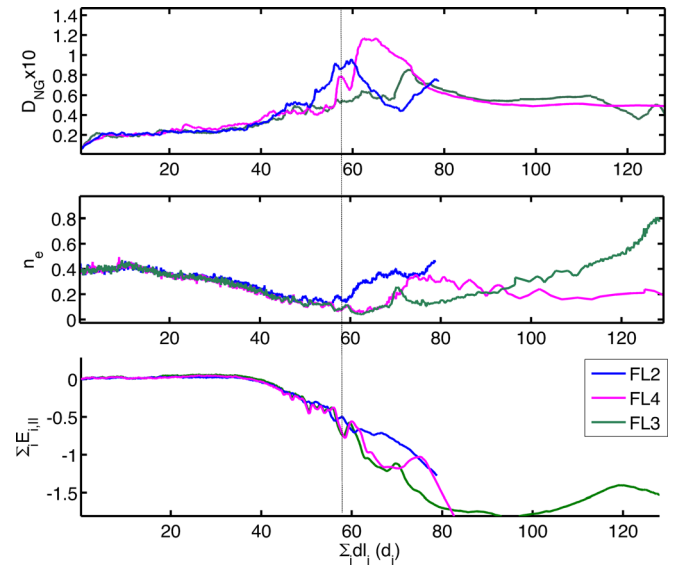

FIG. 7. D_{NG} (top), electron density (middle), and the parallel potential (bottom) as a function of field line length for the three field lines along the inflow (FL 2, FL 3, and FL 4) at which we sample electron distributions. The dashed line marks the center of box 4t, with enhanced D_{NG}.

box 2 (which we will call FL 2) reveals further enhancements in D_{NG} and depletions in n_e at potential wells, for example, between the dashed lines. FL 3 corresponds to the lower nongyrotropy gap between the strips of enhanced nongyrotropy of FL 2 and FL 4 along the inflow (see Fig. 6(b)). While it has larger nongyrotropy than the background, it is much smaller than on FL 2 and FL 4. Nevertheless, it displays the same general correlations between D_{NG}, n_e, and $\varphi_{\parallel}$ as FL 2 and FL 4. These
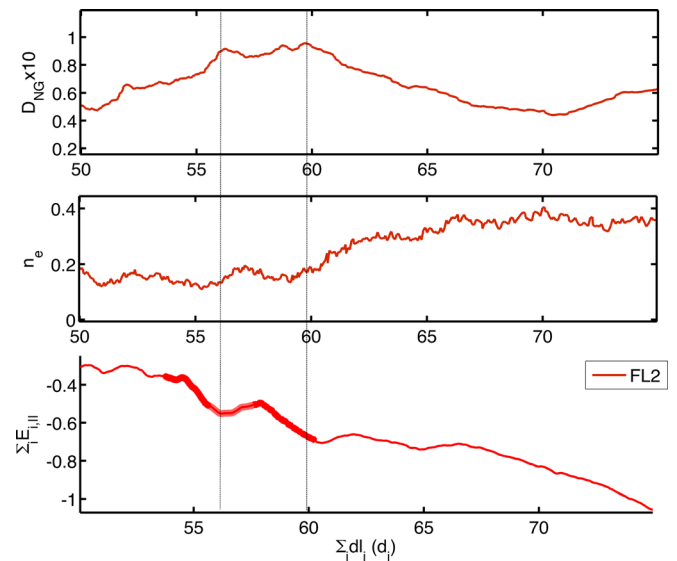

FIG. 8. A magnification of the curves from Fig. 7 that corresponds to FL 2. The highlighted segments show the two locations where we take distributions on this field line. The region between the dashed lines shows the relationship between the electron holes, the density, and the nongyrotropy parameter. Where the parallel potential becomes stronger (more negative) at the holes, D_{NG} shows local enhancement. The density shows enhancements at the boundaries of the holes.
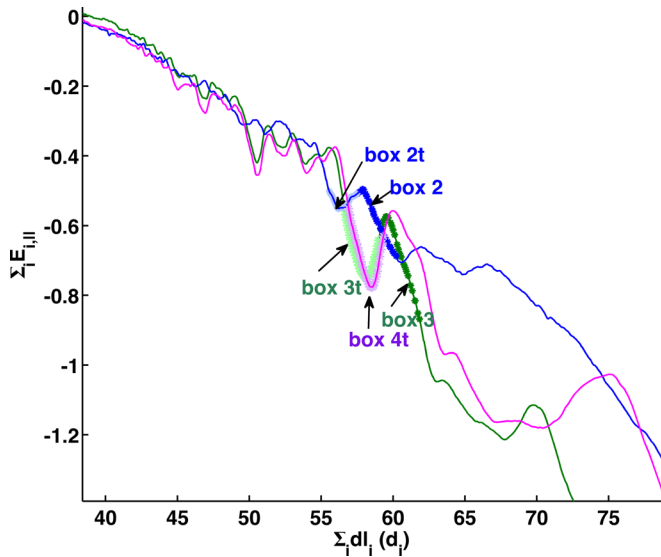
FIG. 9. The potential hills and valleys at the highlighted and labeled successive boxes where we take the distributions along three inflow field lines.

relationships suggest connections between the nongyrotropy and the electron holes and larger scale features of $E_{||}$.

Therefore, on FL 2, 3, and 4, we take a series of successive boxes that align with the potential hills and valleys, as shown by highlighted segments of the parallel potential curves in Fig. 9. The locations of sequential boxes where we will take distributions are distinguished by highlighting in alternating shades and by labels, and there are successive boxes on each field line that correspond to potential hills and wells. FL 2 has not yet reconnected and has a high value of D_{NG}. This field line lies on the lower stripe of large D_{NG}. FL 3 has just reconnected, and at the location of the boxes has a higher D_{NG} than the background, but lower than on adjacent field lines. FL 4 has been reconnected longer than FL 3 and has a high value of D_{NG}. It lies on the upper stripe of high D_{NG} along the inflow. The first distributions that we will discuss belong to the boxes as labeled along the field lines. From each PIC distribution, we will also choose approximately ten particles from within the distribution that have varying velocities and trace their trajectories by integrating backward in time. The particles are chosen to provide good coverage of interesting structures in velocity space. From these trajectories, we will present only those that are characteristic of the observed distribution features in velocity space.
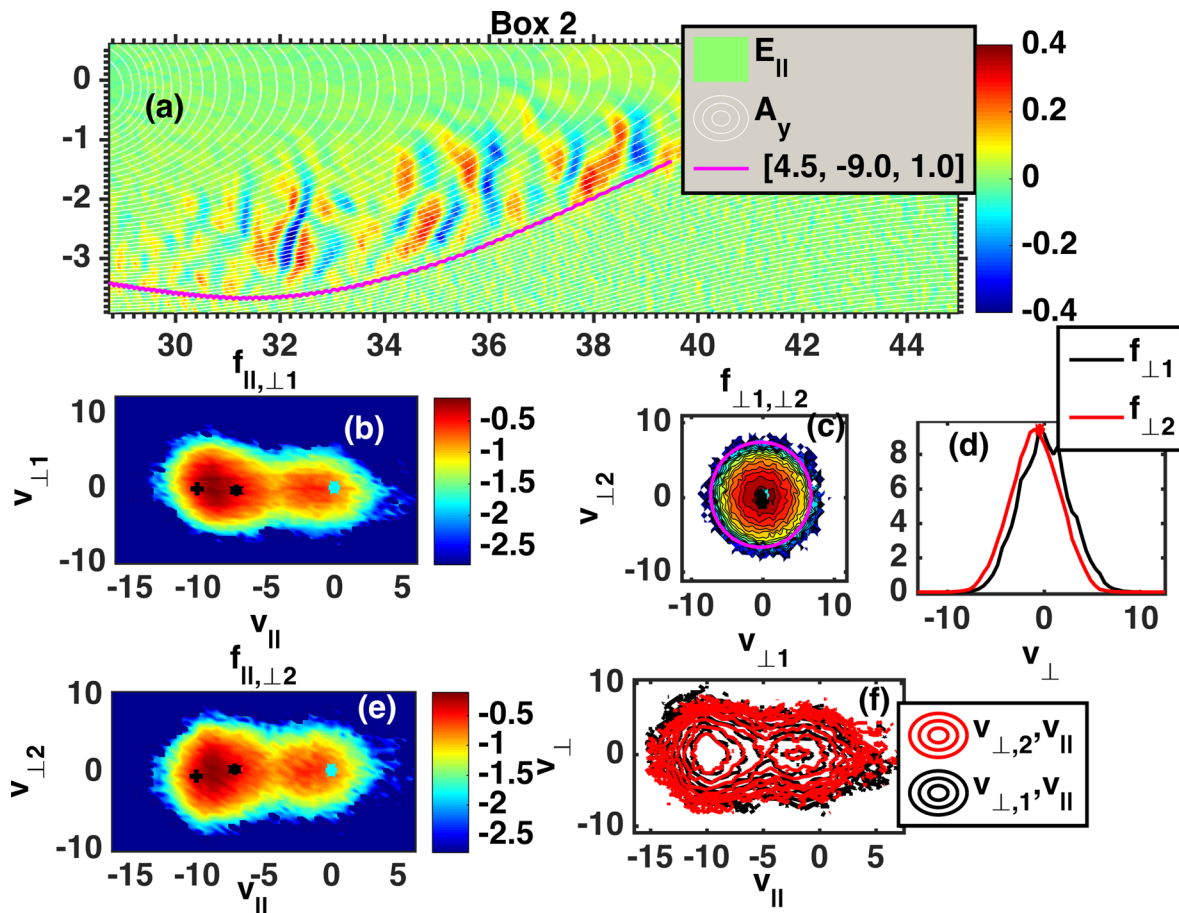

FIG. 10. (a) The trajectory (purple curve) for a particle in the beam population. The background color is the parallel electric field. The bracketed numbers in the legend are the end velocity of the particle chosen for tracing. (b), (c), and (e) The electron distributions in field-aligned coordinates. The black asterisk marks the average velocity of the distribution, and the blue asterisk is the $\mathbf{E} \times \mathbf{B}$ drift velocity. The black cross marks the location of the particle traced backward in time in (a). The parallel beam is composed primarily of particles accelerated from the left side of the simulation domain by the net parallel potential drop. Acceleration by the net parallel potential drop at the location of the box is consistent with the average velocity of the beam. (d) The reduced distributions $f_{\perp,1}$ resulting from summing over $v_{\perp,2}$, and $f_{\perp,2}$ from summing over $v_{\perp,1}$. (f) Overlay of $f_{\perp,1}$ and $f_{\perp,2}$.

We first consider box 2 from FL 2, which is at the location of a potential hill on a field line that has not yet reconnected. There are two populations with distinct statistical features. From tracing a number of particle trajectories within these populations, we find three characteristic histories of the electrons arriving at this location. Figures 10(b), 10(c), and 10(e) show three views of the log of the distribution—two views in the $v_\perp$, $v_\parallel$ plane and one looking along the magnetic field line direction at the $v_{\perp,1}$ $v_{\perp,2}$ plane. Fig. 10(f) shows the contours of the distribution with respect to $v_{\perp,1}|v_\parallel$ (black) and $v_{\perp,2}|v_\parallel$ (red) simultaneously. Fig. 10(d) shows the distributions $f(v_{\perp,1})$ (black) and $f(v_{\perp,2})$ (red) that result from integrating $f(v_{\perp,1}, v_{\perp,2})$ along each of the variables. For the purpose of discussion to come later, the curve for $f(v_{\perp,2})$ has been shifted to the left so that its average matches that of the curve for $f(v_{\perp,1})$. Here, $v_\parallel > 0$ is parallel to **B**, and $v_\parallel < 0$ is antiparallel to **B**. The rotation into field-aligned coordinates are such that the $v_{\perp,1}$ direction lies perpendicular to **B** in the x-y plane, and the $v_{\perp,2}$ direction lies perpendicular to **B** in the plane defined by **B** and z. The black cross marks the velocity in the original x, y, and z coordinates, of the electron selected for the given particle trajectory, the black asterisk marks the average velocity of the distribution, and the blue asterisk corresponds to the **E** × **B** drift velocity. Figs. 10(b) and 10(e) show that the distribution is composed of a field-aligned beam and a slower population with a somewhat different symmetry with respect to the magnetic field direction. The samples of trajectories from the beam population, such as the one shown in Fig. 10(a), are accelerated from the left in toward the x-line, as expected. The estimated average parallel velocity of the beam,

$10.77v_A$, is consistent with acceleration by the parallel potential drop, $11.62v_A$. The high density central part of the slower population tends to belong to particles that have traveled along field lines from the lower right part of the simulation domain and are undergoing reflection (Fig. 11). Particles with smaller $v_\parallel < 0$ than those in the main part of the beam tend to come from two groups. One group includes electrons that have been **E** × **B** drifting and then kicked toward the x-line by encounters with the parallel potential structures, such as shown in Fig. 12. The other group consists of those that, after traveling along field lines from the lower right part of the simulation, have been reflected back toward the x-line by $E_\parallel$ further downstream, as shown in Fig. 13. While these particles may be trapped by the large scale potential, as observed by Egedal *et al.*,[30] they have acquired a boost to the right and are not trapped by the local structure. This is as expected because the location of the box lies on a potential hill, not a potential well.

The distributions in Fig. 10 provide evidence that the electrons are nongyrotropic. Fig. 10(c) shows that the average velocity deviates slightly from the **E** × **B** drift velocity and that the distribution does not coincide with a circle (purple) centered on the mean velocity. Therefore, at least some of the electrons are not simply **E** × **B** drifting. The view with respect to $v_{\perp,1}$ $v_\parallel$ in Fig. 10(b) shows that the deviation of the average velocity from the drift speed occurs in both the beam and the slow population. Fig. 10(b) also shows that the beam population's center of symmetry is clearly offset from that of the slow population. The reduced distributions $f(v_{\perp,1})$ and $f(v_{\perp,2})$ (obtained from integrating over one $v_\perp$ direction) in Fig. 10(d) reveal that neither reduced distribution is symmetric about the mean, since both curves are plotted with
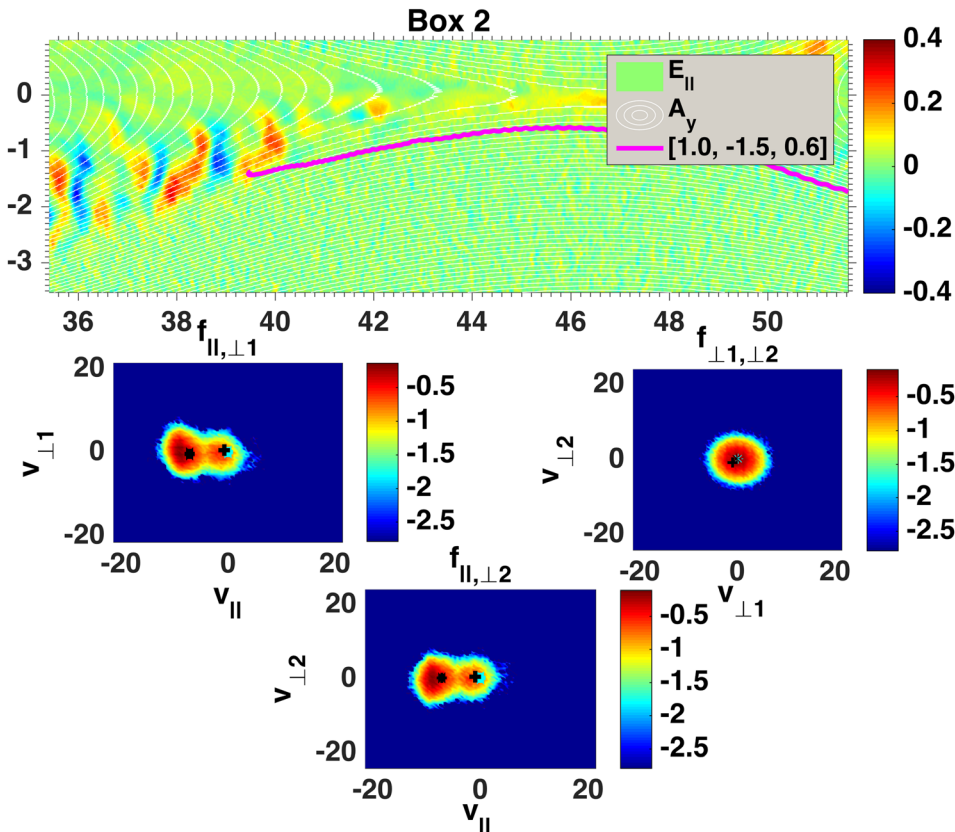

FIG. 11. The slow population consists of electrons that are passing or reflected from the right of the x-line or reflected by $E_\parallel$. Most are getting reflected.

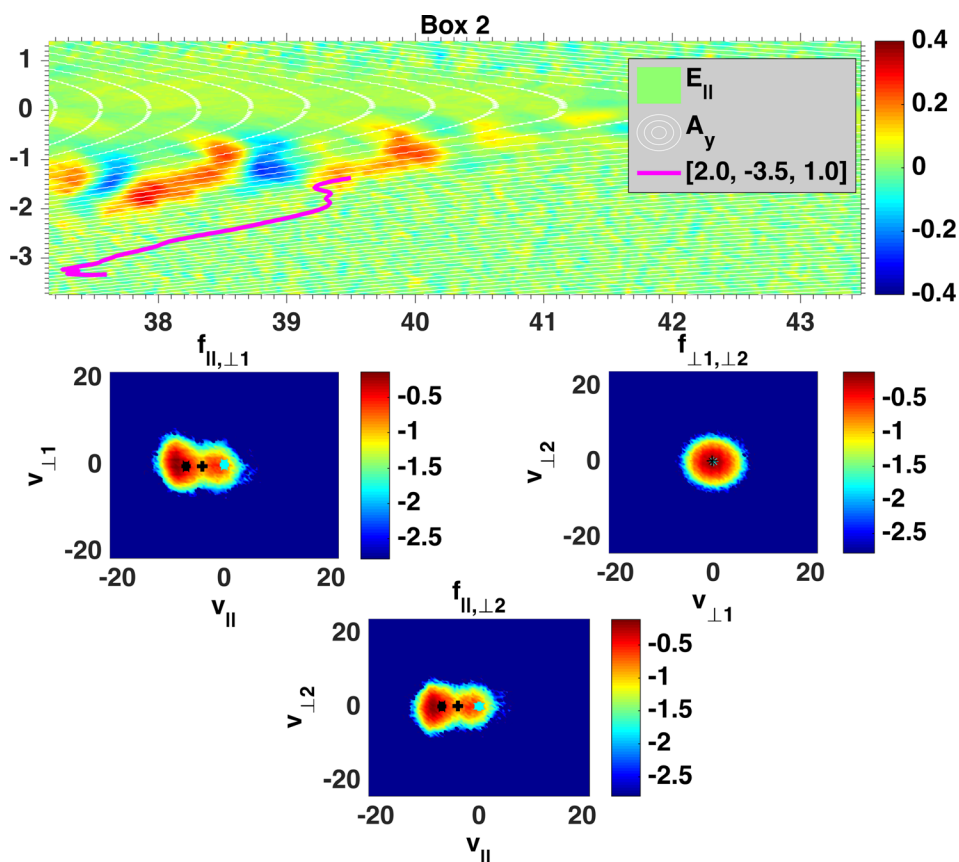FIG. 12. Particles near the edge of both populations with small $v_\parallel < 0$ are sometimes, as here, drifting before getting trapped and kicked toward the x-line.
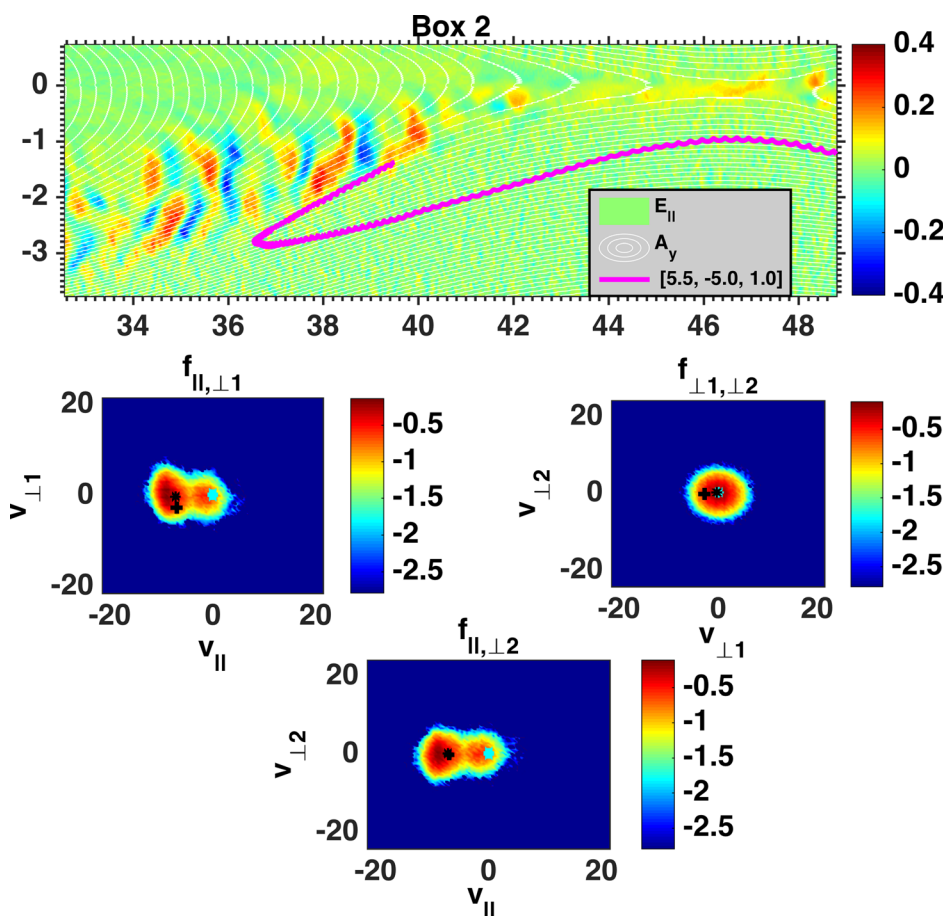

FIG. 13. Some slower particles in the beam population originated on the other side of the x-line and have been reflected by the parallel electric field or possibly mirrored.

respect to a common average (that of $f(v_{\perp,1})$). (If both curves were symmetric about the mean, then they would either overlap or one curve would lie inside the other.) Moreover, their shapes differ from one another, and the shape of the reduced distribution $f(v_{\perp,1})$ is asymmetric about its mean. All of these features signify the distribution's deviation from gyrotropic symmetry about the magnetic field. Fig. 10(f) shows from the overlay of the distributions $f(v_{\perp,1}, v_{\parallel})$ and $f(v_{\perp,2}, v_{\parallel})$ that this asymmetry comes largely from the beam population, though there are asymmetries in the slow population as well. Though subtle, there is a preference for particles with $v_{\perp,1} > 0$ in the beam population, and also a predilection of particles with $v_{\perp,1} > 0$ to have a larger velocity antiparallel to **B**, and that this feature is largely responsible for the nongyrotropy apparent in Fig. 10(c).

There are several sources for the nongyrotropy of the electrons in box 2. These include the influence of the gradients in the electric and magnetic fields and the emf in the gyrocenter coordinates, as discussed earlier. For example, the beam is moving fast enough along the field line that it is possible the electrons are seeing a different magnetic field during a gyroperiod, thus creating an effective gyrophase bunching. The fastest particles would also be most subject to the gradients and curl of $\mathbf{E}_{NI}$, and the fastest particles in the beam show the largest nongyrotropy.

As shown in Fig. 14, the distributions for box 2t, which are on FL 2 but correspond to a local potential well, include the beam and slower populations, but the slower population is more dispersed in velocity than the one in box 2. The trajectories of the slower particles that were traveling from the right are now either reflected as before (Fig. 14), or trapped in the well (Fig. 15), or have enough energy to pass over the potential hill and continue on to the left (Fig. 16). The

trajectory of the trapped particles shows that the electrons that are trapped are reflected once they hit the local well and then bounce back and forth within the well, while they also $\mathbf{E} \times \mathbf{B}$ drift with the field line. The inset to Fig. 15 shows the parallel electric field at the time the particle is initially reflected and trapped and, as expected, shows good correspondence with the location of the reflecting wall of the well at that time. The spread in the slow, trapped population's velocities probably reflects a sloshing back and forth of the particles within the well.

There are indications that the trapped population is nongyrotropic from exposure to the well and that the beam is nongyrotropic. The nongyrotropic asymmetries that characterize the distribution in box 2 appear here as well, as the lack of circular symmetry and the slight deviation from the $\mathbf{E} \times \mathbf{B}$ drift speed attest. The asymmetries in the beam are similar to those in box 2, but now the beam is much narrower in the parallel direction than in box 2. In the slow population, there are very few particles that are either just barely reflected or that have been reflected further away from the x-line. The slow population is less concentrated and includes some particles still moving away from the x-line toward the left. We attribute this to the fact that we are seeing primarily a trapped population and a population that is still moving along field lines from the right that have not been reflected, since this box lies in a well and not on a hill.

The influence of the parallel electric field, the curl and gradients of $\mathbf{E}_{NI}$, and the gradients $\nabla_{\perp}\mathbf{E}_{\perp}\cdot\mathbf{r}_{\perp}$ might be expected to have a stronger effect on the slow population, as it consists primarily of particles trapped by the small-scale local potential well. The trapped particles, for example, are encountering a change in sign of $\partial v_z/\partial z$ at each side of the well. However, at this stage, the trapped particles do not have
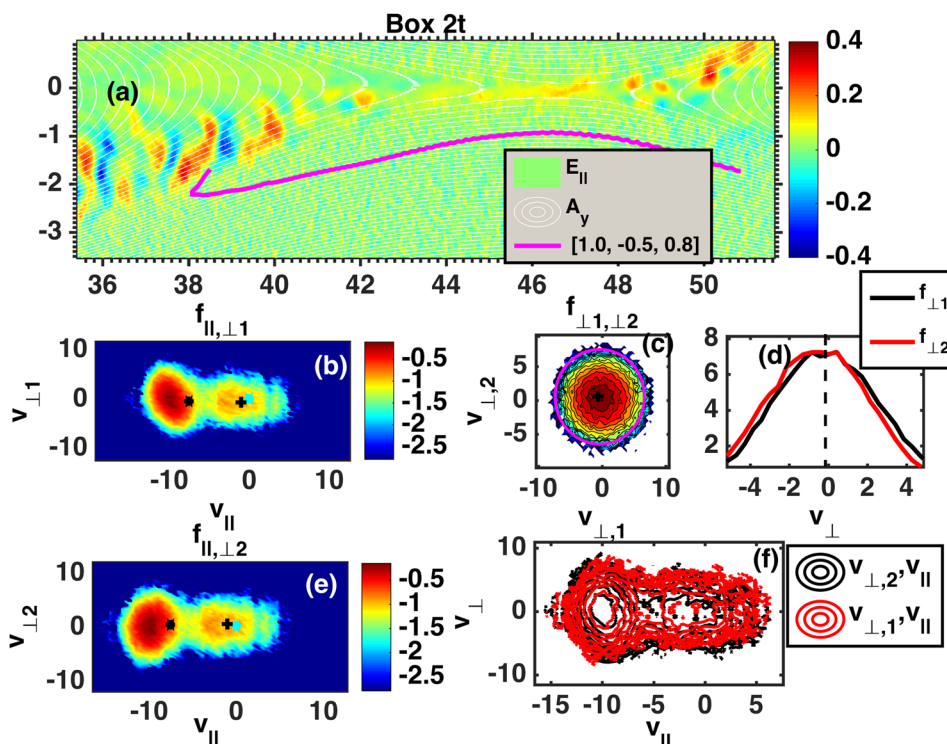

FIG. 14. Some of the slower population particles have been reflected on a trajectory from the other side of the x-line. The average velocity is distinct from the $\mathbf{E} \times \mathbf{B}$ drift velocity.
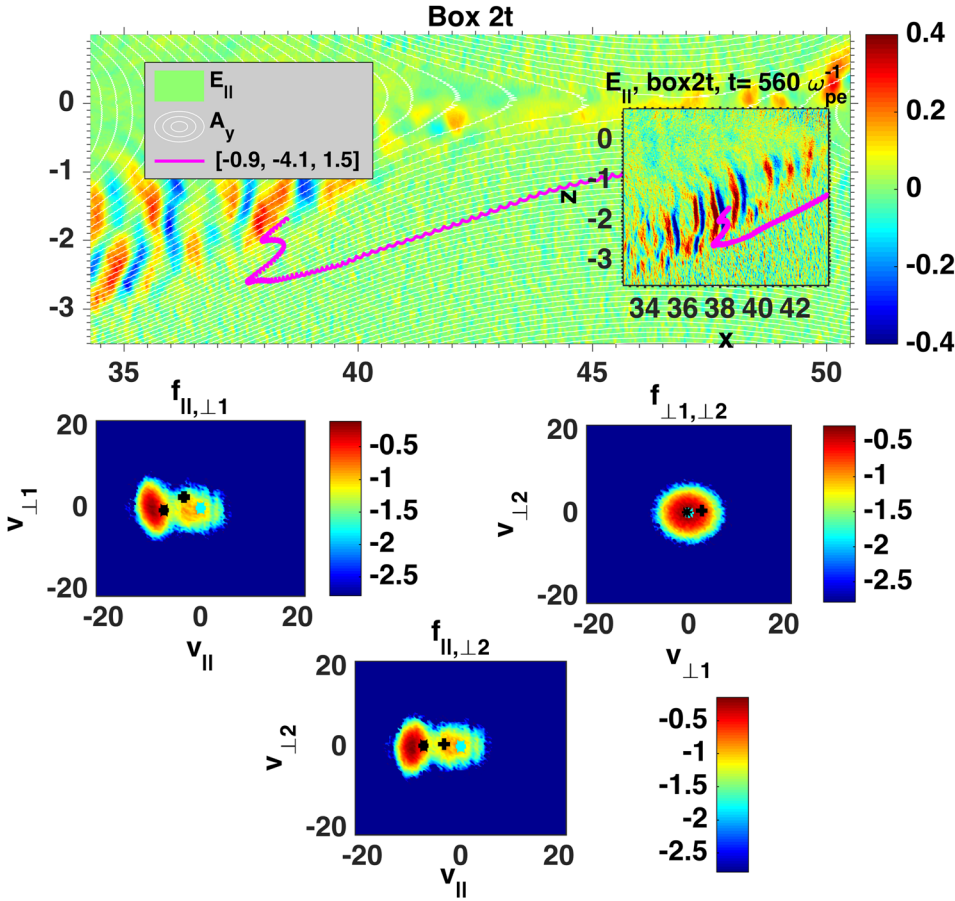
FIG. 15. The slow population now includes a number of trapped particles, such as the electron following the trajectory shown here. The inset shows the parallel electric field at the time the particle is trapped. There is good correlation between the location of the potential well and the location of initial trapping.

strong anisotropy. This may be because the box lies on field lines that have not yet reconnected, and $\mathbf{E}_{NI}$ and its gradients are strongest on field lines that have reconnected (Fig. 4).

The orientation and shape of the beam population support the conclusion that the gradients of the electric field perpendicular to **B** influence the gyroperiod and thus the gyrotropy of the population. For instance, Fig. 14(d) shows that at the lower energies corresponding to the trapped population, $v_{\perp,2} > v_{\perp,1}$. The shape of the distribution is therefore elliptical in the trapped population, with semi-axes that differ by about 20%. Cole[32] predicts the resulting differential drift v_D is given by $v_D = \frac{\omega_c^2}{\omega_{c,eff}^2}\frac{E_0}{B} + v^1\left(1 - \frac{\omega_c^2}{\omega_{c,eff}^2}\right)$, where v^1 is the initial particle thermal speed perpendicular to **B** and to $\delta_\perp \mathbf{E}_\perp \cdot \mathbf{r}_\perp$, and E_0 is the unperturbed background electric field component perpendicular to **B**. The drift is along the direction of v^1. In our case, $v_{\perp,1}$ lies in a direction perpendicular to **B** and the plane defined by **B** and **z**, where **z** is roughly the direction of $\mathbf{V}_\perp \mathbf{E}_\perp \cdot \mathbf{r}_\perp$, and thus corresponds to v^1 in Cole's analysis. Thus, the drift affects particles with different $v_{\perp,1}$ (and different ω) differently. As Cole[32] points out, this is tantamount to a temperature effect on $v_{\perp,1}$. In the rest frame of the drifting electrons, the particle gyrations are elliptical. Because $\mathbf{V}_\perp \mathbf{E}_\perp \cdot \mathbf{r}_\perp$ is in general positive and therefore $\omega_c^2/\omega_{c,eff}^2 < 1$, the theory predicts the radius of the orbits along $v_{\perp,1}$ will be smaller than that along $v_{\perp,2}$ by a factor of $\omega_c/\omega_{c,eff}^2$. These features are therefore consistent with the prediction by Cole[32] for the case of moderate gradients $\mathbf{V}_\perp \mathbf{E}_\perp \cdot \mathbf{r}_\perp$. All of these factors that contribute to the nongyrotropy owe to the electrons' interaction with the parallel and

total nonideal electric field and with field gradients present at the location of the distribution.

FL 3 has just reconnected, and we first look at the distribution of box 3, shown in Fig. 17, located on a potential hill. At this location, there is only a beam with an average parallel velocity of $11.4v_A$ that is accelerated from the left by the potential ramp, which produces a velocity of about $13.6v_A$. There is no slow drifting, passing, or reflected population. We attribute this to the fact that there are no longer new particles arriving from the lower right, since the field line has just reconnected, and there has not yet been enough time for particles injected from the upper half-space to have reached the location. Thus, there is some elevated nongyrotropy within the beam, for the reasons explained earlier, but the value of the nongyrotropy is significantly lower than that of the neighboring field lines because it only has the beam population.

Box 3t, on the other hand, is adjacent to box 3 but lies in a potential well. Therefore, it now hosts an additional trapped population as well as the beam, as we see from Fig. 18. Again, there is a clear preference for $v_{\perp,1} > 0$, suggesting the perpendicular nonideal electric forces affect not only the beam but the trapped electrons as well. The distribution of the trapped population is not symmetric with respect to the $\mathbf{E} \times \mathbf{B}$ drift speed, and thus is not aligned with the average of the faster population. Because the perpendicular components in $\mathbf{E}_{NI}$ tend to be larger where the value of $E_\parallel$ is stronger in the well, this suggests a correlation between the two forces, and therefore may explain the correlation between electrons with larger $v_\perp > 0$ and larger $v_\parallel < 0$. Because of this
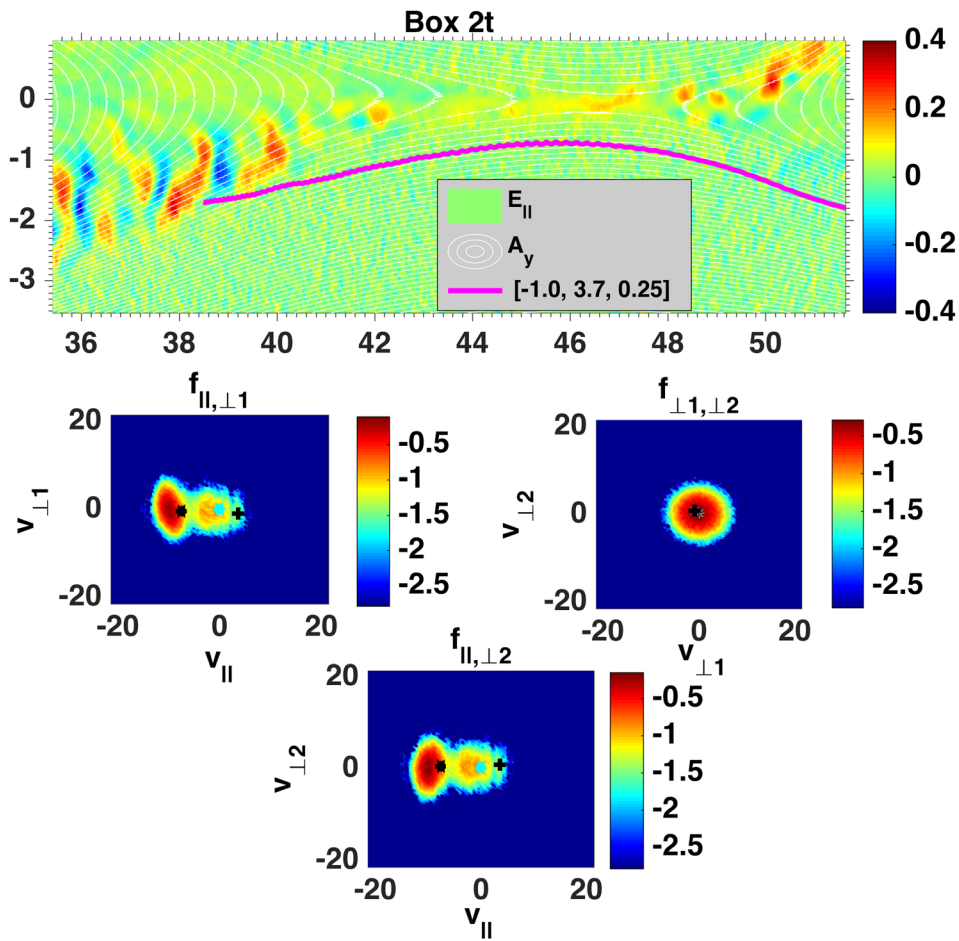
FIG. 16. Particles with $v_{||} > 0$ fly in from the right and have sufficient energy to make it over the well.

nongyrotropy, the value of D_{NG} at this box is higher than that of box 3, as seen in Figures 6 and 7. However, the trapped population is significantly smaller than the trapped population of FL 2, which has not yet reconnected.

Therefore, its value of D_{NG} is still much smaller than that on FL 2. The particles that are trapped, though show much more distortion than in FL 2, which we believe is because the field line has reconnected and now lies in a region with a more
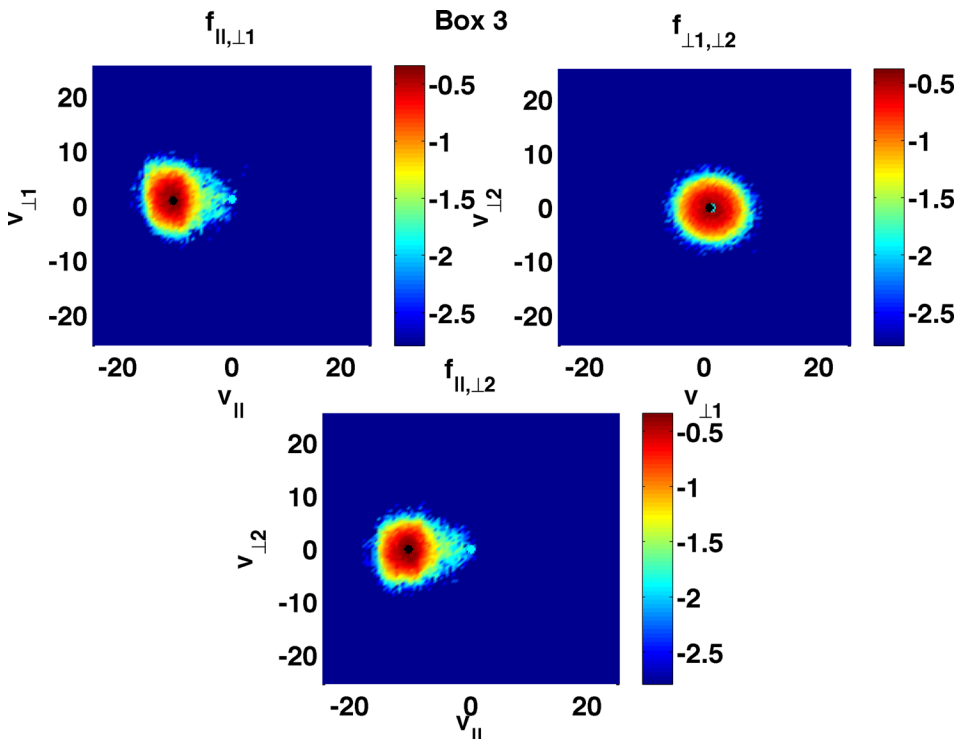

FIG. 17. The nongyrotropy in box 3 is much lower than in the adjacent box 3t, which holds some trapped particles as well, and even lower yet than on FL 2 and FL 4. However, it is higher than the background value, and we can see it is coming from asymmetries in the beam. There is still, for example, a temperature anisotropy between $v_{\perp,1}$ and $v_{\perp,2}$.
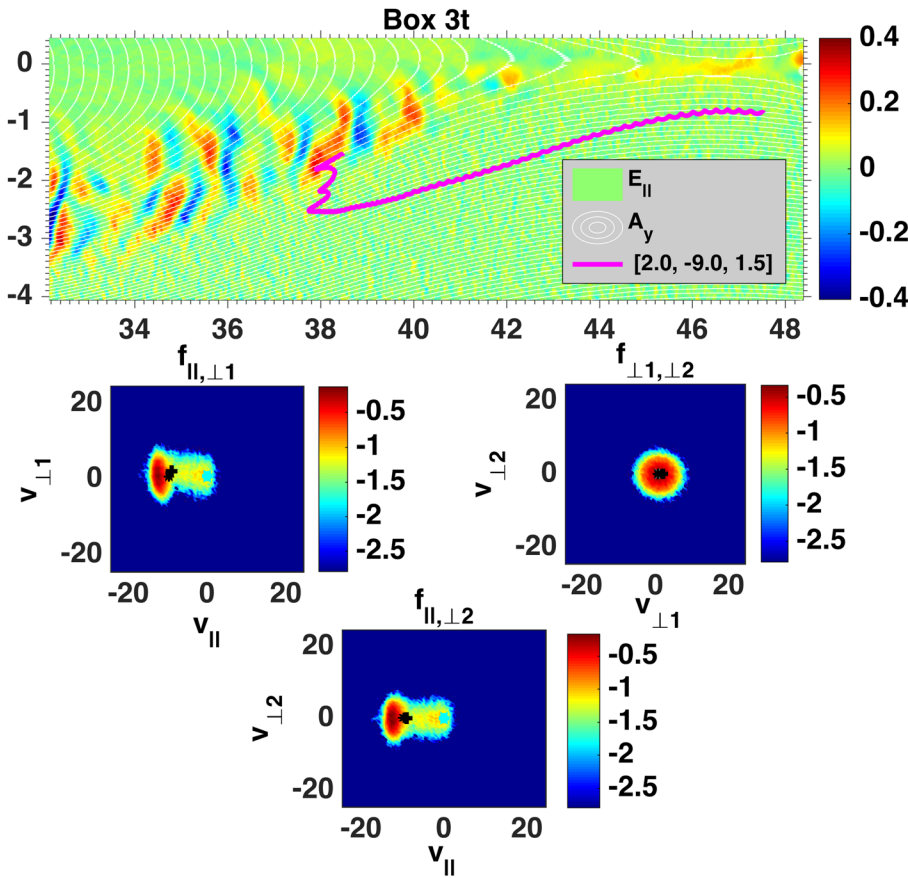
FIG. 18. The well in box 3t has higher nongyrotropy than in box 3, because it has trapped particles, as shown above. However, the density of trapped particles is lower than on FL 2 or FL 4, because FL 3 has just reconnected and new particles are not yet arriving. Therefore, D_{NG} is nevertheless lower than on FL 2 or FL 4.

pronounced $\mathbf{E}_{NI}$. The trapped particles with the highest parallel velocities show the most nongyrotropic distortion, in $v_{\perp,1}$, perhaps a result of the change in the sign of $\mathbf{V} \times \mathbf{E}_{NI}$ in the middle of the box where the trapped particles' $v_{\parallel}$ is greatest. As discussed earlier, this force can produce a change in the gyration speed during an orbit.

FL 4 has been reconnected somewhat longer than FL 3, and again, like FL 2 it sees the highest elevated values of D_{NG}. In Fig. 19, we look at the distribution of box 4t lying on a potential well. Its appearance is very similar to the distribution of box 2t, with a beam and a high density, dispersed trapped population. However, the difference from box 2t is that some of the trapped population consists of electrons that have arrived from the upper left quadrant, since the field line has already reconnected and enough time has passed since then for an influx of particles to arrive from the upper half-plane. Again, the trapped population's lack of gyrotropic symmetry at their larger parallel velocities indicates a possible interaction with the $\mathbf{V} \times \mathbf{E}_{NI}$ and gradients in $\mathbf{E}_{\perp}$ at the potential wells, which is stronger on field lines that have reconnected. Particles that are trapped and those that come from the upper quadrant and have made it past the hill without being reflected (the small population with $v_{\parallel} > 0$) again show a favoritism for $v_{\perp,1} > 0$. The inset to the top panel of Fig. 19 is a magnified view of the end of the trajectory showing that the particle has been reflected. These particles are also not fully magnetized. Electrons entering box 4t from the upper half-plane may have also passed through the diffusion region.

The outflow populations of boxes 7 and 8 are again a collection of electrons from different sources, but now there is

very little localized trapping because the holes are weak in this quadrant. The distribution of box 7, on a field line aligned with the lower strip of heightened D_{NG}, includes electrons that are accelerated away from the x-line and therefore have interacted, either strongly or weakly, with the reconnection electric field. We do not show the trajectories here, but some particles have a moderate velocity parallel to the field line and move in the positive x direction toward the reconnection region. These particles have been drawn in by the larger scale parallel electric field that points outward along the separatrix in the upper left-half-plane, either after $\mathbf{E} \times \mathbf{B}$ drifting downward toward the separatrix or after traveling from the far left of the simulation domain. Also not shown are the trajectories of some particles with $v_x < \approx 0$ that have traveled from the right, accelerated outward by the reconnection electric field, only to be decelerated by the outward $E_{\parallel}$ pointing to the left. Some of the higher energy electrons that have come through the reconnection region originated in the lower right quadrant, after having been reflected by the parallel electric field in the lower left quadrant, as seen in Fig. 20. Other members of the high-energy tail have passed directly through the diffusion region and are strongly accelerated outward (Fig. 21). Fig. 22 shows that the slower particles of the beam population, after drifting toward the reconnection region from the upper half-plane, interact weakly with the reconnection electric field, acquiring an outward acceleration. The members of the high energy tail that have passed directly through the diffusion region form the nongyrotropic part of the distribution and have not yet had time to become fully magnetized on their outward flight.
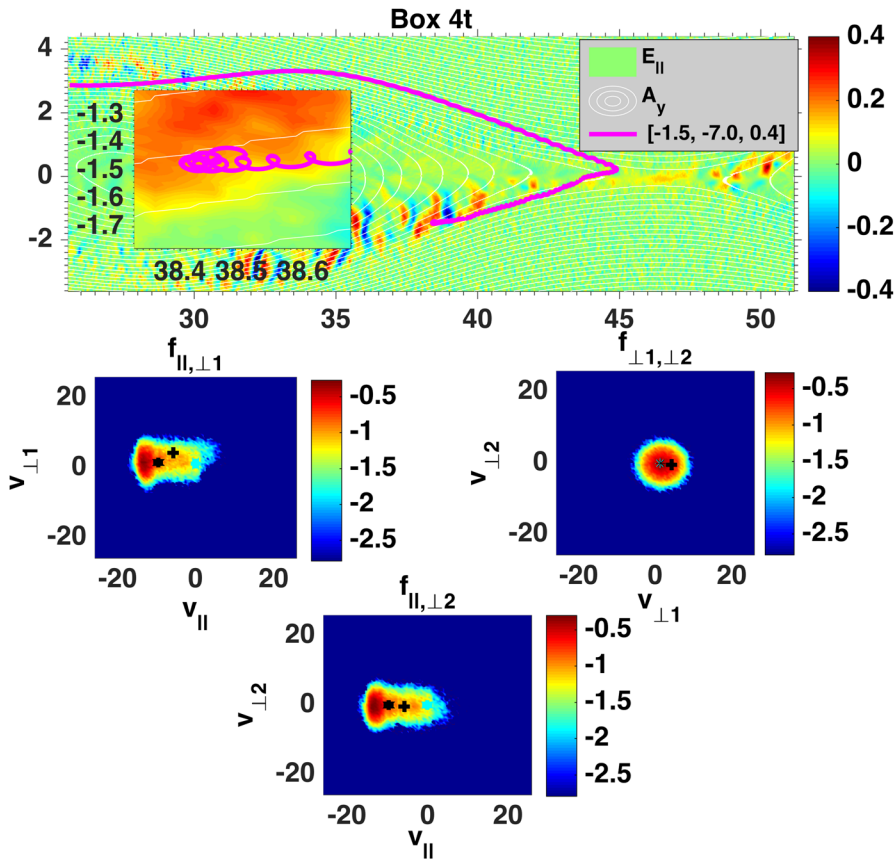
FIG. 19. In box 4t on FL 4, which reconnected earlier than FL 3, some of the trapped/reflected particles arrive from the upper quadrant. The inset in the top panel shows that this particle is actually reflected forward.

The distribution of box 8 on the upper band of high D_{NG} has a similar composition to that of box 7. Both field lines have already reconnected, but FL 7 has reconnected first.

The difference between the distributions in box 7 and box 8 is that in box 8 the highly accelerated electrons in the tail of the distribution come through the diffusion region from the
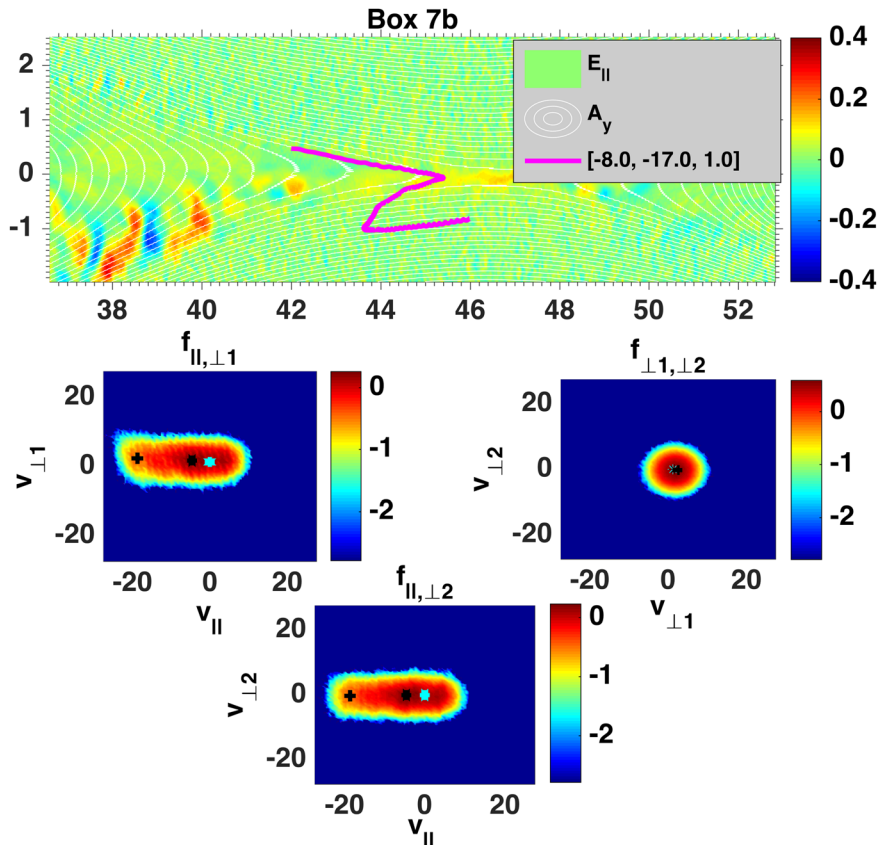

FIG. 20. From this distribution in the outflow, some electrons from the high-speed nongyrotropic part of the tail have passed through the diffusion region from the lower half-plane, after being reflected into the reconnection region.
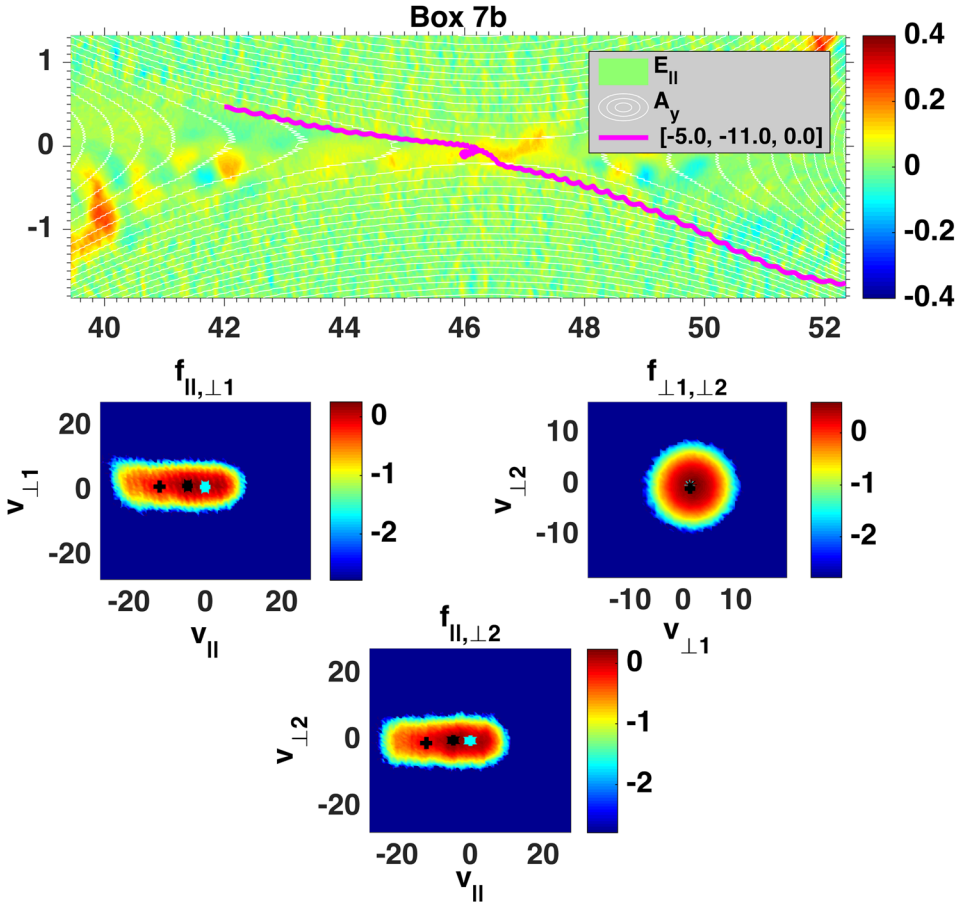
FIG. 21. Some members of the high-speed tail arrive from the lower half-plane and are then accelerated outward by the reconnection electric field.

upper right quadrant rather than the lower right quadrant, as shown by Fig. 23. Again, this population accounts for the nongyrotropic nature of the distribution. Thus, the gap of low nongyrotropy between the two bands of high nongyrotropy along the outflow owes to the delay between the time of flight of the electrons from the lower quadrant and those from the upper right quadrant. Because FL 8 reconnects after FL 7, the particles in box 8 have experienced a shorter time of flight and have perhaps originated their journey before the field line has reconnected. Thus, the particles from the upper right quadrant arrive on any given reconnecting field line earlier than those passing through the reconnection region from the lower quadrant. We comment that the overall, anisotropic structure of the main parallel and perpendicular pressures in the outflow region is consistent with the theory presented in Ref. 35, while the parallel and perpendicular drifts are consistent with those as outlined in the trapping model of Egedal *et al.*[31]

V. NONGYROTROPIC ELECTRONS AND THE PARALLEL ELECTRIC FIELD

Anisotropy of the gyrotropic electron pressure tensor provides a first-order improvement over an isotropic electron pressure to the reconnection equations of state, where the pressure components have been made to balance the large-scale parallel electric field.[35] However, we find that, at least in the case of guide field reconnection, the gyrotropic electron pressure tensor cannot account for the entire parallel electric field on the separatrix with electron inflow and contributes negligibly to

the parallel electric field along the outflow separatrix. Not only are contributions from the nongyrotropic electrons important but the electron inertial terms are as well, showing that even the electron inertial effects can extend along the separatrices.

Fig. 24 plots various contributions to the generalized Ohm's law (grey curves) against the actual total integrated parallel electric field (black curves) and reveals which contributions equate to $E_{||}$ in which domain. The curves represent the net integrated parallel electric field, or contributions thereto, for the field lines that lie on the left hand side of Fig. 3. The electric field has been integrated from the left edge of the simulation domain to the x position of the x-line in Fig. 3. The independent variable is the vertical position z of the endpoints of integration on each field line. In Fig. 24(a), the grey curve represents the gyrotropic electron pressure contribution, $-\int \nabla \cdot \mathbf{P}_{e,G}/(n_e e) \cdot \hat{\mathbf{b}} dl$. While it approaches the value of $\int \mathbf{E} \cdot \mathbf{b} dl$ at some locations in the lower-half plane (the inflow separatrix), the gyrotropic electron pressure contribution does not equate to $\int \mathbf{E} \cdot \mathbf{b} dl$ over the entire region, and accounts for none of $\int \mathbf{E} \cdot \mathbf{b} dl$ in the upper half plane (the outflow separatrix). In Fig. 24(b), the grey curve is the total electron pressure contribution $-\int \nabla \cdot \mathbf{P}_e/(n_e e) \cdot \hat{\mathbf{b}} dl$. The total pressure divergence accounts for most of $\int \mathbf{E} \cdot \mathbf{b} dl$ in the upper half-plane, but overshoots in the lower half-plane. The grey curve in Fig. 24(c) includes the pressure and spatial gradient of the electron inertia, $-\int \nabla \cdot \mathbf{P}_e/(n_e e) \cdot \hat{\mathbf{b}} dl - m_e/e \int \mathbf{v}_e \cdot \nabla \mathbf{v}_e \cdot \hat{\mathbf{b}} dl$, which is again a poor match to $E_{||}$. Finally, in Fig. 24(d), the grey curve captures all contributions to Ohm's law,
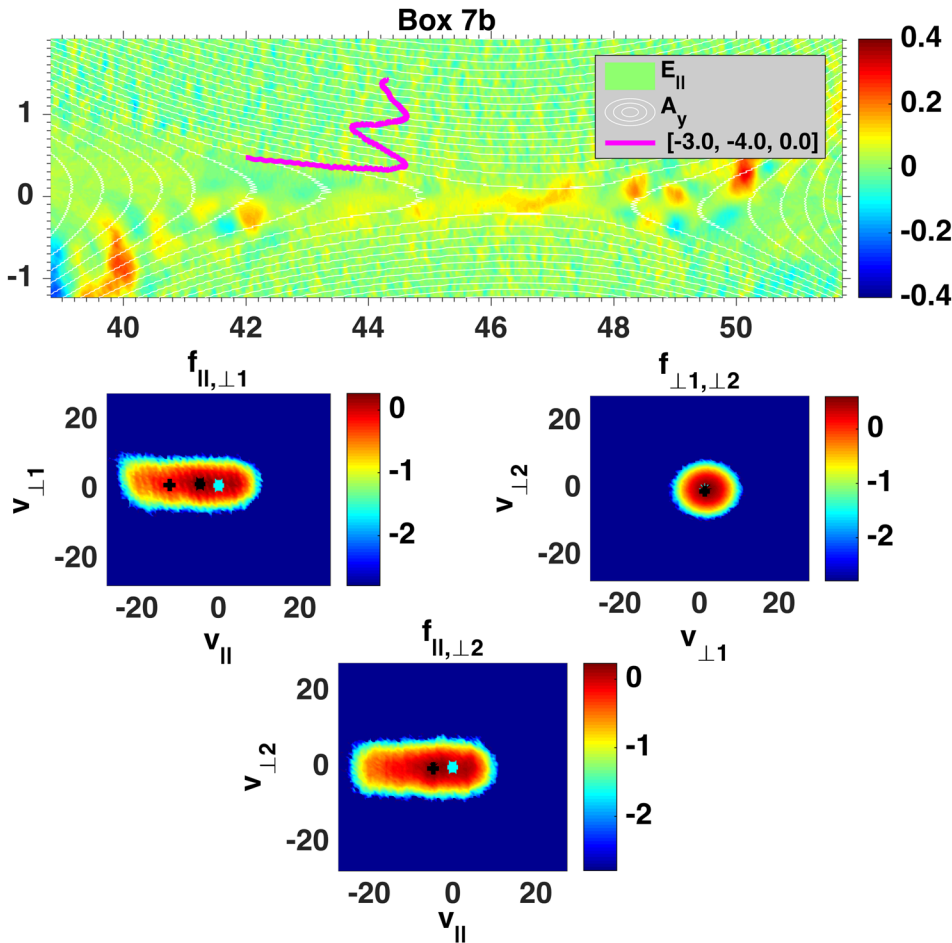
FIG. 22. Some slower members of the high-speed tail have drifted toward the x-line and weakly grazed the reconnection electric field, which accelerates them away from the x-line.

$-\int \nabla \cdot \mathbf{P}_e/(n_e e) \cdot \hat{\mathbf{b}} dl - m_e/e \int (\mathbf{v}_e \cdot \nabla \mathbf{v}_e + \partial \mathbf{v}_e/\partial t) \cdot \hat{\mathbf{b}} dl$. This result shows the best fit to $\int \mathbf{E} \cdot \mathbf{b} dl$, meaning that even electron inertial terms play a role in balancing the large-scale trapping potential. Clearly, all three terms play an important role along the inflow. While the nongyrotropic electron pressure term dominates along the outflow, the inertial terms contribute a small amount there as well. We note that the integrals, which include only the parallel components of $\mathbf{E}_{\mathrm{NI}}$, reflect the fact that there is a net contribution to $\mathbf{E}_{||}$ that persists over the oscillating bipolar structures observed in Figures 2, 4, and 5, as was found in Ref. 36.

VI. SUMMARY

We have demonstrated that the nongyrotropic distributions in the inflow and outflow of guide-field reconnection include multiple populations with different origins and histories. All the populations have all ultimately interacted in some way with the nonideal electric fields and electric field gradients that develop along the magnetic separatrices. As discussed in the Introduction, the large-scale net potential drop and the localized bipolar electron holes have been observed in earlier studies, but here we show they play an important role in producing nongyrotropic electrons. The large-scale parallel electric field accelerates electrons along the field lines to the point that the electrons see a different magnetic field during a gyroperiod. The small-scale parallel

electric field structures both reflect and trap electrons. The beam and the trapped populations deviate from symmetry about **B** and from the $\mathbf{E} \times \mathbf{B}$ drift velocity. The elliptical shape and the orientation of the distributions are consistent with the predictions for nongyrotropic effects from perpendicular gradients of **E.** The nongyrotropy, especially amongst particles along the inflow that have been trapped in the potential wells for a while, is consistent with the presence of nonzero $\nabla \times \mathbf{E}_{\mathrm{NI}}$, where $\mathbf{E}_{\mathrm{NI}}$ is the nonideal electric field, indicating an inductive electric field within the rest frame of the electrons. The sign of the large-scale parallel electric field is consistent with the direction of the reconnection electric field along the separatrix with electron inflow, but not along the separatrix with electron outflow, suggesting different forces balance the parallel electric forces in the two regions. Indeed, comparing the contributions to $E_{||}$ from each term in Ohm's law shows that the all terms are important to balance $E_{||}$ along the separatrices that support electron inflow, even though the total electron pressure tensor dominates $E_{||}$ along the separatrix that supports the electron outflow. This suggests it is possible that $E_{||}$ picks up the total reconnection electric field E_y along the inflow, but not along the outflow. There is also the question of the causal relationship between the nongyrotropic electrons and the parallel electric fields. While the electron nongyrotropy to a large extent balances $E_{||}$, the $E_{||}$ structures may in turn influence or enhance the nongyrotropy. One possible scenario is that the electron holes initiate the
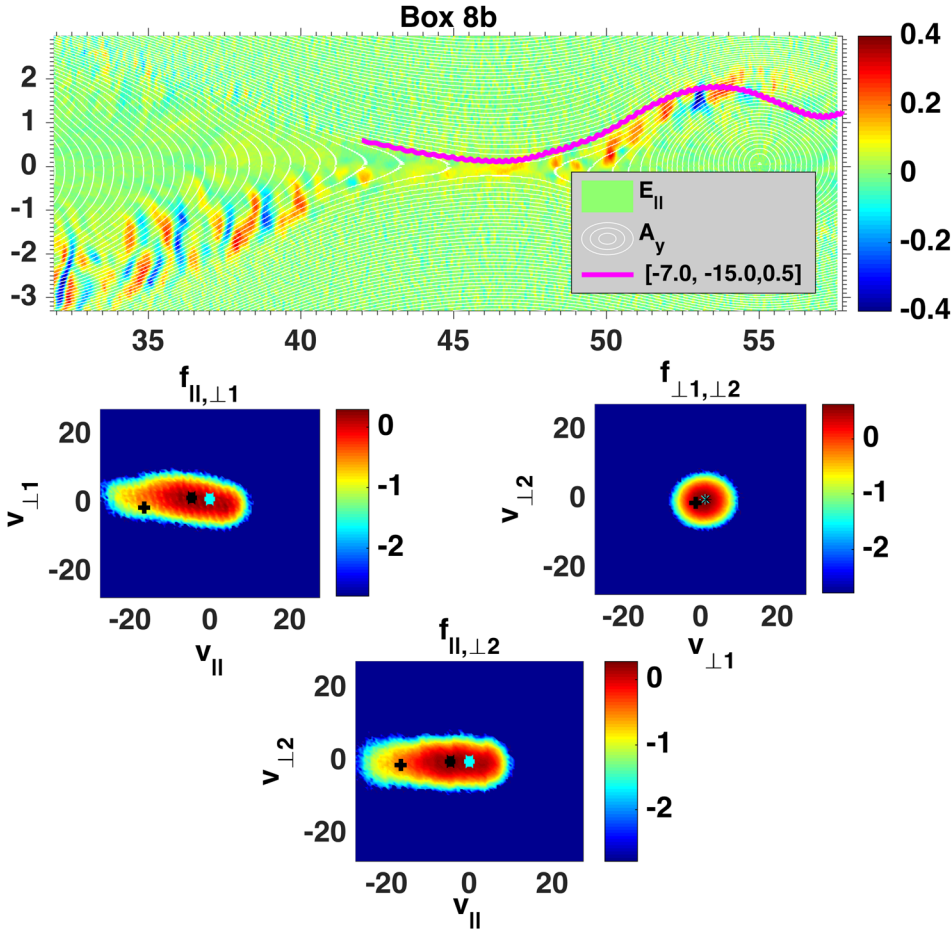
FIG. 23. FL 8 has just reconnected (later than FL 7), and the nongyrotropic high-speed tail of the distribution comes from the upper right quadrant.

nongyrotropy through trapping the electrons, and that the resulting nongyrotropy in turn affects the final nature of $E_{||}$.

Along the separatrices coincident with the electron inflow, the nongyrotropy is elevated both on field lines approaching the reconnection region that have not yet reconnected and on those that have already reconnected. On field lines that have not yet reconnected, there are slower populations that have undergone reflection, and a fast beam accelerated inward by a large-scale parallel electric field. At locations of small-scale potential hills, the electrons are reflected forward without

trapping, and at locations of small-scale potential wells, the particles are trapped within the wells where they bounce. The beam becomes nongyrotropic by virtue of the particles moving fast enough that the magnetic and electric fields change during a gyroperiod. The trapped populations show evidence of non-gyrotropy by their interaction with both the parallel and perpendicular components of the local nonideal electric fields. Furthermore, the gradients in the electric field support an anomalous gyroradius and an anomalous perpendicular drift that varies with perpendicular electron speed (temperature).
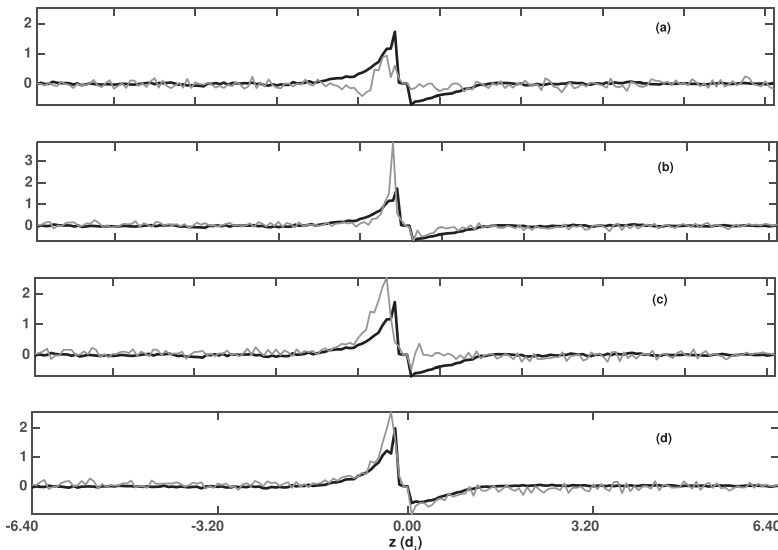

FIG. 24. Comparison of the integrated parallel electric field $-\int_{-\infty}^{l} \mathbf{E} \cdot \hat{\mathbf{b}} dl$ (black curves) to the parallel integral of different terms in Ohm's law (grey curves). The curves represent the net integrated parallel electric field, or contributions thereto, for each of the field lines in Fig. 3, where the field has been integrated from the left edge of the simulation domain to the endpoints shown in Fig. 3. The independent variable is the vertical position z of the endpoints of integration on each field line. (a) The grey curve represents the gyrotropic electron pressure contribution, $-\int \nabla \cdot \mathbf{P}_{e,G}/(n_e e) \cdot \hat{\mathbf{b}} dl$. (b) The grey curve is the total electron pressure contribution $-\int \nabla \cdot \mathbf{P}_e/(n_e e) \cdot \hat{\mathbf{b}} dl$. (c) Here, the grey curve includes the pressure and spatial gradient of electron inertia, $-\int \nabla \cdot \mathbf{P}_e/(n_e e) \cdot \hat{\mathbf{b}} dl - m_e/e \int \mathbf{v}_e \cdot \nabla \mathbf{v}_e \cdot \hat{\mathbf{b}} dl$. (d) Here, the grey curve captures all contributions to Ohm's law, $-\int \nabla \cdot \mathbf{P}_e/(n_e e) \cdot \hat{\mathbf{b}} dl - m_e/e \int (\mathbf{v}_e \cdot \nabla \mathbf{v}_e + \partial \mathbf{v}_e/\partial t) \cdot \hat{\mathbf{b}} dl$.

This effect potentially impacts all particles that come into contact with it.

In the inflow on field lines that have just reconnected, there is a much lower degree of nongyrotropy than on adjacent field lines, though it is still larger than in the background. Though within local potential wells there are some trapped electrons, there are much fewer than on field lines that have not yet reconnected and still receive a supply of particles from the lower right quadrant. The field line has not been reconnected long enough for particles from the upper half plane to reach the location. Thus, the trapped/reflected population is much lower on these field lines, and therefore, the nongyrotropy is lower. The lower population of trapped electrons relative to that in wells on field lines that have not yet reconnected begs the question of whether some of the trapped electrons manage to escape the small-scale wells. A similar location on field lines that have been reconnected somewhat longer starts to receive particles from the upper half plane, which provide the new source for trapped and reflected populations. Thus, there is a gap of lower D_{NG} between layers of elevated D_{NG} owing to a time-of-flight effect.

Within the outflow regions, the large-scale parallel potential and the diffusion region affect the particles more than the small-scale structures, because the holes are weak there. Nongyrotropy is elevated on field lines that have already reconnected. On field lines that have just reconnected, nongyrotropic distributions consist of populations of particles that drift in from above and glance through the diffusion region, of those that are reflected back toward the x-line, and of those that come from the upper right inflow and are highly accelerated from passing through the diffusion region (e.g., FL 8). On field lines that have reconnected somewhat earlier (e.g., FL 7), the nongyrotropic distributions consist of similar populations, but this time the highly accelerated beams have originated in the lower half-plane before passing through the diffusion region. In both cases, the highly accelerated beams that have encountered the reconnection electric field are still not fully magnetized and are responsible for the nongyrotropy. Thus, again there is a time-of-flight effect that produces a filament of lower nongyrotropy between layers of very elevated nongyrotropy.

To briefly summarize, we have found a relationship between nongyrotropic electrons and large and small-scale parallel electric fields. The small-scale electric fields are electron holes that are most pronounced along separatrices aligned with inflowing electrons, and a large-scale parallel field whose in-plane component emanates away from the reconnection region along all separatrices. The gyrotropic pressure shears are insufficient to balance the parallel electric fields. Along the separatrix with inflowing electrons, all terms in the generalized Ohm's law are required to balance the observed large-scale parallel potential. Along the separatrix with outflowing electrons, the parallel electric field is largely balanced by the entire electron pressure tensor divergence with a small contribution from the time-dependent electron inertia. These characteristics have important implications for detecting the inflow and outflow separatrices in observations of guide-field reconnection. However, we note

that importance of these nonideal terms along the separatrices may diminish with an increasing mass ratio. Both the small and large-scale parallel electric structures trap electrons. Along the separatrices supporting inflow, the gradients in the electric field and the non-conservance of magnetic flux contribute to the nongyrotropy. Along the separatrices with outflowing electrons, particles have passed through the reconnection region and are not yet fully remagnetized. With guide field reconnection, nongyrotropy and the forces that produce it are therefore present beyond the electron diffusion region. They are accentuated also along the magnetic separatrices, heralding important implications for theory and observations of magnetic reconnection.
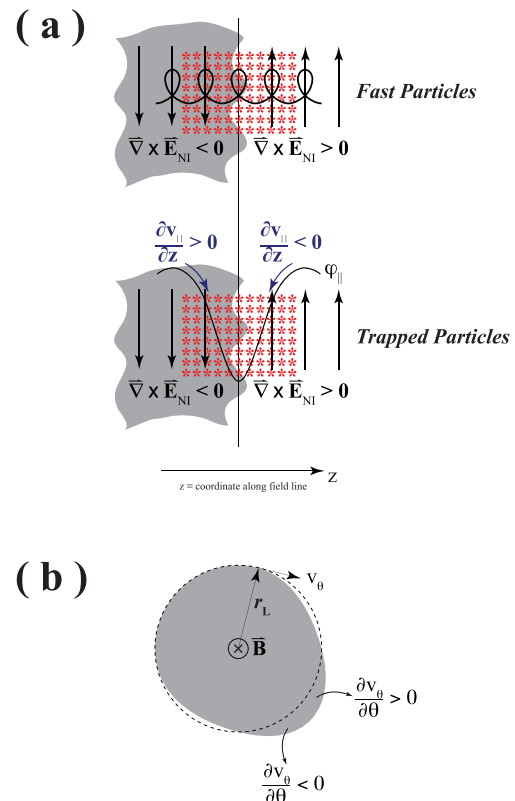
APPENDIX: NONGYROTROPY THROUGH $\nabla \times E_{NI}$

FIG. 25. (a) Particles with large v_z (velocity parallel to B) encounter a boundary in the rotational nonideal field E_{NI} (top) when crossing the middle of the electron hole and entering the collection box (red) within the hole (here a potential well). Thus, they gyrate through a reversal in the sign of $\nabla \times E_{NI}$ as they accelerate over the electron hole. Particles with smaller $v_{||}$ that oscillate within the well (middle figure) of an electron hole will experience a reversal in $\nabla \times E_{NI}$ at their peak parallel velocity in the center of the well and a reversal in $\partial v_z/\partial z$ at the edges of the well. (b) Distributions that already have a nongyrotropy and a $\partial v_\theta/\partial \theta$ will undergo an increase in v_θ on one side of the distortion, where $\partial v_\theta/\partial \theta > 0$, and a decrease where $\partial v_\theta/\partial \theta < 0$.

[1]M. Hesse and K. Schindler, J. Geophys. Res. **93**(A6), 5559–5567, doi:10.1029/JA093iA06p05559 (1988).

[2]M. Hesse, T. G. Forbes, and J. Birn, Astrophys. J. **631**, 1227–1238 (2005).

[3]M. Hesse, M. Kuznetsova, and J. Birn, Phys. Plasmas **11**, 5387 (2004).

[4]M. Hesse and D. Winske, J. Geophys. Res. **103**, 26479–26486, doi:10.1029/98JA01570 (1998).

[5]M. Hesse, J. Birn, and M. Kuznetsova, J. Geophys. Res. **106**(A3), 3721–3735, doi:10.1029/1999JA001002 (2001).

[6]M. Hesse, K. Schindler, J. Birn, and M. Kuznetsova, Phys. Plasmas **6**, 1781–1795 (1999).

[7]H. Karimabadi, W. Daughton, and J. Scudder, Geophys. Res. Lett. **34**, L13104, doi:10.1029/2007GL030306 (2007).

[8]V. M. Vasyliunas, Rev. Geophys. Space Phys. **13**(1), 303–336, doi:10.1029/RG013i001p00303 (1975).

[9]L.-J. Chen, N. Bessho, B. Lefebvre, H. Vaith, A. Fazakerley, A. Bhattacharjee, P. A. Puhl-Quinn, A. Runov, Y. Khotyaintsev, A. Vaivads, E. Georgescu, and R. Torbert, J. Geophys. Res.: Space Phys. **113**, A12213 (2008).

[10]J. D. Scudder, R. D. Holdaway, W. S. Daughton, H. Karimabadi, V. Roytershteyn, C. T. Russell, and J. Y. Lopez, Phys. Rev. Lett. **108**, 225005 (2012).

[11]N. Aunai, M. Hesse, and M. Kuznetsova, Phys. Plasmas **20**, 092903 (2013).

[12]M. Hesse, Phys. Plasmas **13**, 122107 (2006).

[13]M. M. Kuznetsova, M. Hesse, and D. Winske, J. Geophys. Res. **106**(A3), 3799–3810, doi:10.1029/1999JA001003 (2001).

[14]P. L. Pritchett and F. S. Mozer, J. Geophys. Res. **114**, A11210, doi:10.1029/2009JA014343 (2009).

[15]J. Scudder and W. Daughton, J. Geophys. Res. **113**, A06222, doi:10.1029/2008JA013035 (2008).

[16]J. R. Shuster, L.-J. Chen, W. S. Daughton, L. C. Lee, K. H. Lee, N. Bessho, R. B. Torbert, G. Li, and M. R. Argall, Geophys. Res. Lett. **41**, 5389, doi:10.1002/2014GL060608 (2014).

[17]F. J. R. Simões, M. V. Alves, F. R. Cardoso, and E. Costa, J. Atmos. Sol.-Terr. Phys. **73**, 1511 (2011).

[18]J. F. Drake, M. Swisdak, C. Cattell, M. A. Shay, B. N. Rogers, and A. Zeiler, Science **299**, 873 (2003).

[19]P. L. Pritchett and F. V. Coroniti, J. Geophys. Res. **109**, A01220, doi:10.1029/2003JA009999 (2004).

[20]C. Cattell, J. Dombeck, J. Wygant, J. F. Drake, M. Swisdak, M. L. Goldstein, W. Keith, A. Fazakerley, M. André, E. Lucek, and A. Balogh, J. Geophys. Res. **110**, A01211, doi:10.1029/2004JA010519 (2005).

[21]J. F. Drake, M. A. Shay, W. Thongthai, and M. Swisdak, Phys. Rev. Lett. **94**, 095001 (2005).

[22]J. Egedal, M. Øieroset, W. Fox, and R. P. Lin, Phys. Rev. Lett. **94**, 025006 (2005).

[23]J. R. Wygant, C. A. Cattell, R. Lysak, Y. Song, J. Dombeck, J. McFadden, F. S. Mozer, C. W. Carlson, G. Parks, E. A. Lucek, A. Balogh, M. André, H. Rème, M. Hesse, and C. Mouikis, J. Geophys. Res. **110**, A09206, doi:10.1029/2004JA010708 (2005).

[24]M. V. Goldman, D. L. Newman, and P. Pritchett, Geophys. Res. Lett. **35**, L22109, doi:10.1029/2008GL035608 (2008).

[25]A. Divin, G. Lapenta, S. Markidis, D. L. Newman, and M. V. Goldman, Phys. Plasmas **19**, 042110 (2012).

[26]K. Fujimoto, Geophys. Rev. Lett. **41**(8), 2721–2728 (2014).

[27]J. Egedal, W. Daughton, A. Le, and A. L. Borg, Phys. Plasmas **22**, 101208 (2015).

[28]J. Egedal, W. Daughton, and A. Le, Nat. Phys. **8**, 321 (2012).

[29]C. C. Haggerty, M. A. Shay, J. F. Drake, T. D. Phan, and C. T. McHugh, Geophys. Res. Lett. **42**(22), 9657–9665, doi:10.1002/2015GL065961 (2015).

[30]J. Egedal, W. Daughton, J. F. Drake, N. Katz, and A. Le, Phys. Plasmas **16**, 050701 (2009).

[31]J. Egedal, A. Le, and W. Daughton, Phys. Plasmas **20**, 061201 (2013).

[32]K. D. Cole, Planet. Space Sci. **24**, 515–518 (1976).

[33]V. See, R. F. Cameron, and S. J. Schwartz, Ann. Geophys. **31**, 639–646 (2013).

[34]D. P. Stern, J. Geophys. Res. **78**(10), 1702, doi:10.1029/JA078i010p01702 (1973).

[35]A. Le, J. Egedal, W. Daughton, W. Fox, and N. Katz, Phys. Rev. Lett. **102**, 085001 (2009).

[36]D. E. Wendel, D. K. Olson, M. Hesse, N. Aunai, M. Kuznetsova, H. Karimabadi, W. Daughton, and M. L. Adrian, Phys. Plasmas **20**, 122105 (2013).